MANUFACTURING OF COPPER COLD PLATES VIA METAL FUSED FILAMENT FABRICATION AND THEIR CHARACTERIZATION

A THESIS SUBMITTED TO
THE GRADUATE SCHOOL OF NATURAL AND APPLIED SCIENCES
OF
MIDDLE EAST TECHNICAL UNIVERSITY

BY

MEHMET CANBERK BACIKOĞLU

IN PARTIAL FULFILLMENT OF THE REQUIREMENTS
FOR
THE DEGREE OF MASTER OF SCIENCE
IN
MECHANICAL ENGINEERING

JANUARY 2023

Approval of the thesis:

MANUFACTURING OF COPPER COLD PLATES VIA METAL FUSED FILAMENT FABRICATION AND THEIR CHARACTERIZATION

submitted by **MEHMET CANBERK BACIKOĞLU** in partial fulfillment of the requirements for the degree of **Master of Science in Mechanical Engineering Department, Middle East Technical University** by,

Prof. Dr. Halil Kalıpçılar
Dean, Graduate School of **Natural and Applied Sciences** _____

Prof. Dr. M. A. Sahir Arıkan
Head of Department, **Mechanical Engineering** _____

Assoc. Prof. Dr. Ulaş Yaman
Supervisor, **Mechanical Engineering, METU** _____

Examining Committee Members:

Prof. Dr. Serkan Dağ
Mechanical Engineering, METU _____

Assoc. Prof. Dr. Ulaş Yaman
Mechanical Engineering, METU _____

Assoc. Prof. Dr. Özgür Bayer
Mechanical Engineering, METU _____

Assoc. Prof. Dr. Kıvanç Azgın
Mechanical Engineering, METU _____

Prof. Dr. Oğuzhan Yılmaz
Mechanical Engineering, Gazi University _____

Date: 26.01.2023

I hereby declare that all information in this document has been obtained and presented in accordance with academic rules and ethical conduct. I also declare that, as required by these rules and conduct, I have fully cited and referenced all material and results that are not original to this work.

Name, Surname: Mehmet Canberk Bacıkoğlu

Signature :

ABSTRACT

MANUFACTURING OF COPPER COLD PLATES VIA METAL FUSED FILAMENT FABRICATION AND THEIR CHARACTERIZATION

Bacıkoğlu, Mehmet Canberk
M.S., Department of Mechanical Engineering
Supervisor: Assoc. Prof. Dr. Ulaş Yaman

January 2023, 74 pages

Unlike traditional manufacturing methods, Additive Manufacturing (AM) is one of the most popular methods to produce parts with complex geometries using a wide range of materials. Atomic Diffusion Additive Manufacturing (ADAM) is an AM method to manufacture metal parts by using filaments which include metal powders encased in plastic binders. Various types of materials can be 3D printed with this method, including stainless steel, copper, tool steel, Inconel, and titanium. In this study, ADAM method is used to manufacture cold plates with interior channels used to cool down circuit boards for electronic applications. Before the fabrication of cold plates, test parts that replicate some parts of the cold plates are manufactured to characterize material properties and control the quality of initial parts. CMM measurements, surface roughness measurements, Micro-CT and X-ray scans, density determination with Archimedes method, SEM analysis, and thermal conductivity measurements are conducted on the test parts. Then, interior channels are generated with different cross sections considering supportless manufacturing where the liquid stream passes. drop and temperature mapping of the cold plates manufactured with copper are observed with experiments. According to the results, the lowest pressure

drop is obtained for the cold plate with triangle cross-section. Cold plate with droplet cross-section has the minimum temperature value on the resistor and has the highest performance rating among the other cold plates manufactured via ADAM method. This design approach shows that ADAM can be used for its speed and wide range of materials, and can be adapted for various fast-prototyping industries that require complex interior channels in mechanical parts.

Keywords: atomic diffusion additive manufacturing, cold plate, interior liquid channel, channel cross-section, material characterization, quality control

ÖZ

BAKIR SOĞUK PLAKALARIN METAL ERGİYİK FİLAMENT İLE İMALAT YÖNTEMİ İLE ÜRETİLMESİ VE KARAKTERİZASYONU

Bacıkoğlu, Mehmet Canberk
Yüksek Lisans, Makina Mühendisliği Bölümü
Tez Yöneticisi: Doç. Dr. Ulaş Yaman

Ocak 2023 , 74 sayfa

Eklemeli İmalat, geleneksel üretim yöntemlerinin aksine, karmaşık geometriye sahip parçaları çeşitli malzemeler kullanarak üretebilme kabiliyetinden dolayı günümüzdeki en popüler üretim yöntemlerinden biridir. Atomik Difüzyon Eklemeli İmalat (Atomic Diffusion Additive Manufacturing, ADAM), plastik bağlayıcıyla çevrelenmiş metal tozlarından oluşan filametler kullanarak metal parçaların üretilmesini sağlayan bir eklemeli imalat yöntemidir. Bu yaklaşım ile paslanmaz çelik, bakır, takım çeliği, Inconel ve titanyum gibi malzemeler kullanılarak parçalar üretilebilir. Bu çalışmada, devre kartlarını soğutmada kullanılan kanallı soğuk plakaların üretiminde ADAM yöntemi kullanıldı. Soğuk plaka üretiminden önce, malzeme özelliklerini karakterize etmek ve parça kalitelerini kontrol etmek için soğuk plakaların bazı kısımlarını yansıtan test parçaları üretildi. Test parçaları kullanılarak CMM ölçümleri, yüzey pürüzlülüğü ölçümleri, Mikro-CT ve X-ray taramaları, Arşimet yöntemiyle yoğunluk testi, SEM incelemeleri ve termal iletkenlik ölçümleri yapıldı. Sonrasında, desteksiz üretim prensibi düşünülerek farklı kanal kesitleri içeren sıvı kanalı yapıları tasarlandı. Üretilen bakır soğuk plakaların basınç düşümü ve sıcaklık dağılımı değişkenleri de-

neyler ile incelendi. Sonuçlara göre, kanal kesidi üçgen olan soğuk plakada en düşük basınç düşümü elde edildi. Damla kanal kesitli soğuk plakada direncin üstündeki sıcaklıkların en düşük olduğu ve performans değerlendirmesinin ADAM yöntemi ile üretilen diğer soğuk plakalara kıyasla daha iyi olduğu gözlenmiştir. Bu tasarım yaklaşımının sonuçlarına göre, ADAM yönteminin hız ve geniş malzeme çeşitliliği gibi avantajları sayesinde karmaşık iç kanallı mekanik parçaların üretileceği, hızlı prototipleme gereken çeşitli endüstriyel uygulamalarda kullanılabileceği görülmüştür.

Anahtar Kelimeler: atomik difüzyon eklemeli imalat, soğuk plaka, iç sıvı kanalı, kanal kesidi, malzeme karakterizasyonu, kalite kontrol

To my family

ACKNOWLEDGMENTS

I would like to express my sincere gratitude to my supervisor Prof. Dr. Ulaş Yaman for his guidance, encouragement, patience, and help. I would also like to thank Prof. Dr. Serkan Dağ, Assoc. Dr. Özgür Bayer, Assoc. Dr. Kıvanç Azgın and Prof. Dr. Oğuzhan Yılmaz for being on my jury and expressing their very useful comments and suggestions.

I am grateful to my company ASELSAN Inc. for letting and supporting my thesis. I also wish to present my special thanks to Murat Çetin, Oğuz Doğan, Vedat Yağcı, and Ahmet Şahin Şen for their experience and insights that enlightened me throughout this study.

I present my thanks to Prodigma Teknoloji Inc. and Tolga Bolol for their assistance and support in the manufacturing processes.

I would like to thank Dilay Güleryüz for her inspiration, help, support, and patience.

Lastly, I would like to express my deepest thanks to my family for their endless support, love, and faith.

TABLE OF CONTENTS

LIST OF TABLES

TABLES

LIST OF FIGURES

FIGURES

LIST OF ABBREVIATIONS

ABBREVIATIONS	
3D	3 Dimensional
ABS	Acrylonitrile Butadiene Styrene
ADAM	Atomic Diffusion Additive Manufacturing
AM	Additive Manufacturing
BCC	Body-Centered Cubic
BJ	Binder Jetting
BMD	Bound Metal Deposition
CAD	Computer Aided Design
CFD	Computational Fluid Dynamics
CNC	Computer Numerical Control
CMM	Coordinate Measuring Machine
CT	Computed Tomography
DED	Directed Energy Deposition
DMLS	Direct Metal Laser Sintering
EBM	Electron Beam Melting
FCU	Flow Control Unit
FDM	Fused Deposition Modeling
FFF	Fused Filament Fabrication
FSW	Friction Stir Welding
HEX	Heat Exchanger
LPBF	Laser Powder Bed Fusion
M-FFF	Metal Fused Filament Fabrication

NDT	Non-destructive Testing
PCB	Printed Circuit Board
PLA	Polylactic Acid
RF	Radio Frequency
SEM	Scanning Electron Microscopy
SLA	Stereolithography
SLM	Selective Laser Melting
SLS	Selective Laser Sintering
SS	Stainless Steel
TIG	Tungsten Inert Gas
TPMS	Triply Periodic Minimal Surfaces

CHAPTER 1

INTRODUCTION

1.1 Motivation and Problem Definition

Radar and electronic systems contain electronic units, cards, and components that dissipate high thermal loads. Since those electronic entities must work under a temperature limit to give optimum performance, the system must be kept under temperature limits. Various cooling units must be used to ensure the maximum temperature limit of the system and cool down the electronic units. Cold plates are one of the main cooling elements in radar systems because of their efficiency in cooling and easy assembly interface for modular radar structures. Electronic units, Printed Circuit Boards (PCBs), Radio Frequency (RF) modules, and antenna cards can be located on radar structures by assembling them on cold plates. Since radar structures are large mechanical systems, a great number of cold plates can be used in them.

There are some limits in producing cold plates with traditional methods. Since cold plates are complex parts, only few manufacturing methods can be used such as brazing, Friction Stir Welding (FSW), and Tungsten Inert Gas (TIG) welding. These unique methods focus on bonding two parts together which have details of channel and fin structures on. By joining these parts, an interior channel of a cold plate can be formed. Then, with machining operations, final geometries and assembly interfaces for electronic units can be obtained.

Stated joining methods are part-specific traditional manufacturing methods that are commonly used in electronic cooling applications but limit fabrication in some terms. For example, design of cold plates is limited by joining methods, the chosen method can limit the channel cross sections, outer dimensions, and channel paths. Computer

Numerical Control (CNC) machining is also needed both before and after the joining process to shape the cold plate to the final form which affects production costs and timings negatively, resulting in serious problems in manufacturing. In addition to these, used materials are limited mostly to some series of aluminum.

1.2 Proposed Methods and Models

Additive Manufacturing (AM) technologies are evolved as a new branch manufacturing of intricate parts with more freedom in design and material. Alternative manufacturing methods are considered in terms of advantages to eliminate bottlenecks and limits in traditional methods.

By using Atomic Diffusion Additive Manufacturing (ADAM) method [1], which is a new AM approach, an alternative way for cold plate manufacturing is proposed in this thesis. Different liquid channel cross-sections are designed and evaluated in terms of thermal performance. Copper material is chosen to build cold plates because of its high thermal conductivity compared to aluminum, a commonly used material in traditional manufacturing methods. 3 Dimensional (3D) printing times and costs are also affected positively by using the ADAM method in production when compared to the traditional manufacturing methods.

1.3 Contributions and Novelties

The contributions and novelties of the thesis are as follows.

- Copper cold plates with four different channel cross-sections are designed and manufactured with the ADAM method.
- Channels are generated considering supportless manufacturing inside the channel.
- With material characterization tests and quality control methods, the ADAM technique is evaluated to be used in thermal applications.

- Basic machining operations on copper cold plates are done.
- Cold plates are evaluated experimentally in terms of thermal performance.

1.4 The Outline of the Thesis

In Chapter 2, background information for the study is provided, and the relevant works in the literature are reviewed and discussed. In Chapter 3, design, manufacturing, characterization, and control of test parts are presented. In Chapter 4, details about the design and manufacturing of cold plates are explained, then experimental tests of cold plates in terms of thermal performance are covered. In Chapter 5, the work is brought to a conclusion.

CHAPTER 2

BACKGROUND & LITERATURE REVIEW

In this chapter, background information about thesis and the state of the art in related topics are provided.

2.1 Metal Fused Filament Fabrication Method

Metal Fused Filament Fabrication (M-FFF) is one of the AM methods that is used to manufacture metal parts by using filaments composed of metal powders encased in plastic binders [2]. It is advantageous for lower device and operation costs and for manufacturing parts with complex geometries using a wide range of materials, including stainless steel, copper, tool steel, nickel alloys, and titanium.

M-FFF process has three main steps to obtain the final part after designing the part. Designed parts must be subjected to some post-processing to obtain the final part. Parts designed in Computer-Aided Design (CAD) software must be prepared to be printable on a M-FFF type of 3D printer (Figure 2.1). In M-FFF systems, the desirable part is manufactured larger than the desired part considering the removal of plastic material in the metal filaments. This scaling is performed on the Computer-Aided Manufacturing (CAM) software. Before fabricating the part, the nozzle head automatically maps and levels the bed to ensure the quality of the first layer. After printing the part, obtained product is called as green part due to its lower strength and loose connection between the extruded beads. Then, the green part is washed and binder is removed and the brown part is obtained, which has high porosity due to the removed binders. Later on, the brown part is located in an oven for the sintering process. Dimensions of the brown part decreases and sintering of metal material are

developed and the final part is obtained. To obtain uniform shrinkage and prevent warping during the sintering operation, the part is fabricated on a raft geometry made of the same material as the desired part. A thin layer of ceramic powder between the green part and the raft helps to separate parts by applying lower forces, such as hitting with a hammer slightly on the piece.

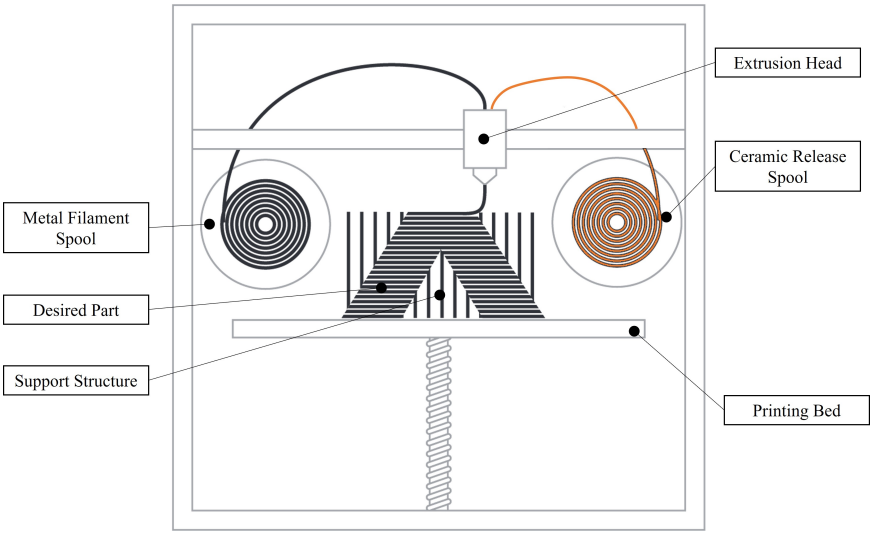

Figure 2.1: Schematic of M-FFF printer adapted from [1].

Obtaining various metal parts in a cheaper way than Selective Laser Melting (SLM) process is possible with the M-FFF approach. Although production times can be longer than other AM methods, an accessible range of materials for the end-use parts or fast prototyping in a low-cost system are the major advantages of the M-FFF. Complex parts can be printed in the M-FFF system on the condition that the part fits into the build volume.

2.2 Cold Plates

Cold plates are the most effective cooling components where liquid cooling is necessary rather than air cooling since there happens high heat dissipation in some systems. High-power electronic units, PCBs, phased array antennas and batteries are the main systems where cold plates are used to cool down structures and to eliminate exceeding temperatures above the defined temperature limit in the system. To cool down

the system, liquid passes through channel/channels of the cold plates with required flow parameters which are usually determined after Computational Fluid Dynamics (CFD) analysis. More functional and effective cold plates with interior channels can be designed according to the results of the CFD analysis which represents the effects of the important parameters related to the suitability of the part and returns the design parameters of structures [3]. Temperature distribution, pressure drop, heat dissipation, channel height and width, and channel route in the structure are the critical parameters that affect the cold plate design.

In conventional manufacturing methods of cold plates, such as brazing and FSW (Figure 2.2), the cross-section of the channel is generally selected as rectangular shape because of the easiness of manufacturing on CNC milling machines. To increase thermal performance and route liquid, fins can be added to the interior channels. On the other hand, most of the different channel cross sections other than rectangular shapes and complex interior channels cannot be produced with the conventional methods. Customized cold plates such as multiple-storeyed, tile structured, or organic shaped can be produced only with the AM methods. Therefore, AM methods are valuable options to manufacture more efficient and intricate cold plates. However, there are some criteria to be determined before the manufacturing process. Since there will be flowing liquid inside of the cold plate, channel geometry must be produced without supports, and the orientation of the part during printing must be arranged according to it. In addition to this, support structures printed inside of the part cannot be easily removed after manufacturing. Therefore, the interior channel must be printed without any support structures to obtain the desired flow. The size of the print bed must also be kept in mind in the first step of the design process since it can be a limiting factor for larger cold plate applications.

2.3 Material Characterization

To characterize the properties of the newly used materials, some tests can be conducted to find material properties such as density [4], porosity, thermal conductivity, etc. Tests must be operated according to the regulated standards in the industry. These standards are prepared according to related materials, methods, and procedures by

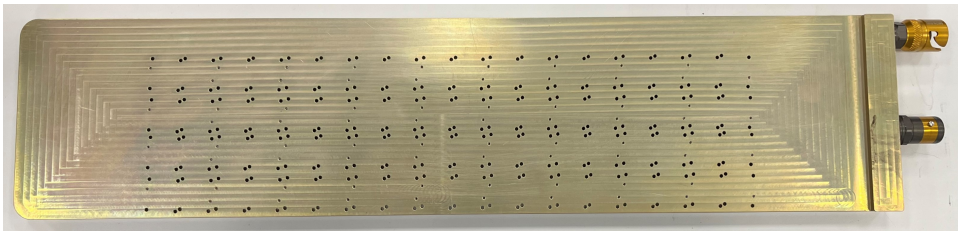

(a) Cold plate manufactured with brazing.

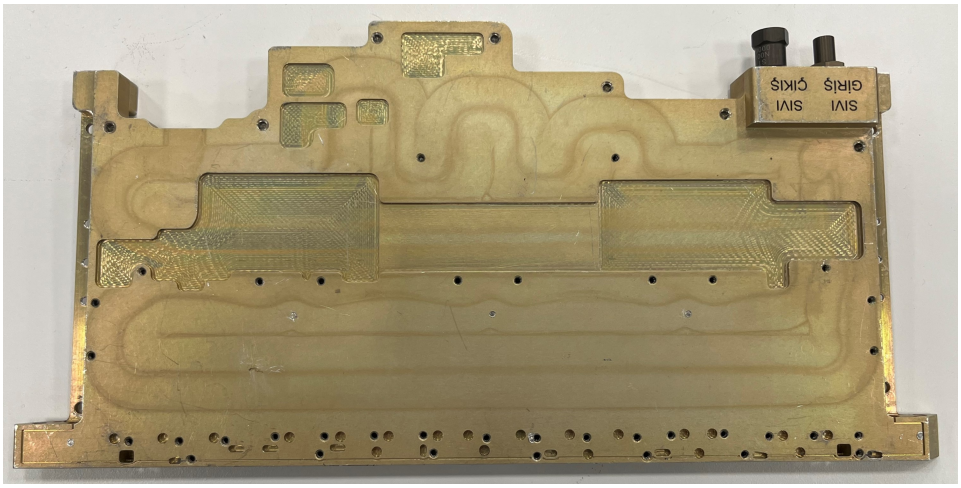

(b) Cold plate manufactured with FSW.

Figure 2.2: Some examples of cold plates manufactured with traditional methods.

committees and specialists around the world. Results, obtained after material characterization processes, guide design processes such as manufacturing method, material selection, and operation limits.

2.4 Quality Control

For critical products to be used in various applications, some validations must be conducted. According to the quality requirements in various industries, required tests, controls and analyses must be performed. These steps can be conducted according to the settled standards or functional requirements of products. Destructive testing or Non-Destructive Testing (NDT) methods can be performed for products according to the requirements. For end-use parts, NDT methods are the initial validation steps to be applied. Parts manufactured with traditional methods or with AM methods

share some common NDT methods for validation such as the Coordinate Measuring Machine (CMM) process, Micro-Computed Tomography (CT), surface analyses, and X-ray scanning. Dimensional tolerances and dimensional accuracy of parts can be determined by using CMM [5]. X-ray and Micro-CT scans are very beneficial tools to control the internal structure of materials where some excess material such as support structures in AM or chips in traditional manufacturing methods may exist. The Micro-CT method is also a helpful method to observe the porosity and diversity of materials inside a part. Measuring surface roughness is critical to control the quality of the surface where two parts will be assembled together and convenient contact between them is necessary. Surface roughness requirements are much more achievable in subtractive manufacturing methods than in AM methods. In AM methods, surface roughness criteria must be evaluated more meticulously and design and process parameters must be determined accordingly.

2.5 Literature Review

AM is a method that is used to manufacture complex parts with a completely novel approach compared to the traditional manufacturing methods [6]. Since AM has more freedom than the other manufacturing processes, AM technologies are utilized more frequently in the industry day by day. With AM, most of the limitations in traditional machining can be eliminated, pushing the limits of design, creativity, and effectiveness in manufacturing. Furthermore, rapidity and affordability are other critical properties of AM that would create an innovative path for cutting-edge technologies and products.

Polymer-based materials and metal powders constitute two major branches in AM when raw materials are considered. According to the desired material and function of the parts, several AM methods can be used. Fused Filament Fabrication (FFF) is one of the most popular AM methods that extrudes material through a nozzle and constructs a part layer by layer. Mostly polymer-based materials such as Acrylonitrile Butadiene Styrene (ABS) and Polylactic Acid (PLA) can be produced via this method, but more specific materials such as ULTEM, copper, tool steel, etc., can be added to the manufactured product material range using enhanced 3D printers. On

the other hand, SLM [7] is a process that various types of materials in powder form are distributed over a dynamic table and melted by a high-power laser to bond powders to each other layer-by-layer according to the 3D geometric model of the desired part. After fusing step is finished, some post-processes such as machining, surface finishing, heat treatment, sandblasting, etc. are applied and the final part is obtained [8]. In SLM, parts can be manufactured with aluminum alloy powders, steel powders such as maraging steel, stainless steel, titanium alloys, etc. These materials can be selected according to the application area, structural requirements, corrosion levels, thermal properties, etc. [9].

Manufacturing parts with interior channels is challenging due to the design and production criteria. By using traditional methods such as conventional welding, brazing, and FSW, structures with interior channels can be produced in a limited manner. With the help of recent advancements in AM, especially in SLM, manufacturing limitations have been decreased. Complicated, cost-effective, and functional parts can be produced as end-use artifacts [10]. Manufacturing of these parts with multi-staged conventional methods reduces freedom in design. SLM can produce structures that have voids inside due to the advantageous properties of the process itself [11]. More functional and effective parts with interior channels can be obtained with parameter optimization of AM machinery [3]. Temperature distribution, pressure drop, heat dissipation, channel height and width, and channel route in the structure are some parameters that affect design and help the designer to generate the optimal design. Cost functions [12] for specific parameters or density-based optimization [13] approaches can be conducted during the part optimization process. Interior structures can also be optimized in the manner of flow characteristics or mass reduction by using lattice, Body-Centered Cubic (BCC) [14], Voronoi [15] or Triply Periodic Minimal Surfaces (TPMS) structures. These complex structures with various channel geometries are able to be manufactured thanks to the abilities of AM.

As mentioned, the SLM method is highly preferable for metal part production in AM. But a newly developed process called M-FFF is an alternative approach for metal part production. Developments and studies about this alternative approach show that M-FFF has great potential in metal production. For example, in the study of Henry et al. [16] presented the printing of 17-4 PH Stainless Steel (SS) via the ADAM method on

a Markforged Metal X 3D printer. Anisotropic behavior is discussed in the paper after conducting shear, tensile, and bending tests. Different test parts are manufactured with varying orientations of 3D printing. It is shown that the material response is sensitive to the extrusion paths and porosity is measured as 3.3% with Scanning Electron Microscopy (SEM). Rodriguez et al. [17] used copper with the Metal X 3D printer by Markforged. The electrical and mechanical properties of pure copper after manufacturing with the ADAM method are measured in the work. The density of pure copper is measured with three methods which are Archimedes, micrography, and X-ray. The relative density of pure copper is found to be lower than 95% which is worse than the other two AM technologies, SLM and Electron Beam Melting (EBM). Lower electrical conductivity, yield, and tensile strength are measured in the parts compared to the parts manufactured with SLM. Although surface roughness results are found to be lower in ADAM than in SLM, machining operations are still needed as post-processing. For tensile tests, ISO 6892-1 is used, and machined parts showed worse structural properties than the built ones. Removal of the contour layer, defective machining of the parts, and incipient cracks after machining could be the reasons for these results. It is stated that enhancements and optimization in the ADAM process can improve relative density, which could improve copper's mechanical and electrical properties. Galati and Minetola [18] characterized the ADAM process. A Markforged Metal X 3D printer is used, and parts are manufactured with 17-4 PH SS material for analysis. Dimensions of the green parts and the sintered parts were measured with a micrometer, and the deviation range was reported. The densities of parts were measured using the Archimedes method. Surface roughness results were measured by using a profilometer. Dimensional accuracy was observed using a CMM on a reference artifact, and evaluation was done according to ISO 286-1:1988. Relative density was around 90% for the sintered parts, which was far lower than the published values. For smaller cubes, Ra values were measured as 1.5μm and 3.1μm for top and vertical surfaces; for bigger cubes, Ra values were measured as 9.5μm and 9.1μm for top and vertical surfaces. For sizes up to 120 mm, artifact quality corresponds to IT12 and IT13 classes in ISO ranges. Finishing operations must be performed to obtain desired surface finish and accuracy.

Cold plates are one of the key components of some electronic devices such as high-

power electronics [19][20], phased array antennas [21][22] etc. to cool down the structures that may bear high thermal loads. These structures are very much like to the heat exchangers (HEXs) which include interior channels where cooling liquid passes through [23][24]. Cooling liquid flow paths have prime importance in these structures to cool down the components effectively while providing convenient structural strength and mass [25]. Various AM methods such as SLM, Selective Laser Sintering (SLS), EBM, Stereolithography (SLA), and FFF are used to manufacture HEXs. For example, in the study of Boxleitner et al. [26], a HEX is produced with the FFF method by using carbon fiber-filled polyamide filament. The conductivity of carbon fiber-filled polyamide material is measured with the laser flash method and is used in CFD analysis of the HEX to compute the heat transfer rate and the pressure drop. Unsatisfying results are acquired for the HEX manufactured with AM than commercially available HEX. Defects can also lead to leakages. The discontinuous in the extrusion process can be a reason for these defects and it could be an obstacle when water tightness is considered. As stated in the study, continuous bead means that deposition without stopping, and multiple contours to form a thicker wall can improve water tightness. In addition to these, pressure drop according to the experimental measurement is 90%, higher than the predicted results in Direct Metal Laser Sintering (DMLS), but in the FFF process, experimental measurement is 20% higher than the predicted results which is a direct result of better surface roughness in FFF compared to DMLS. A compact HEX is produced via SLA by using PlasGRAY V2 photopolymer resin in the work of Dixit et al. [27]. Gyroid lattice structures are used for TPMS patterning in HEX and the smallest feature size is kept as 300μm. Since the wall thickness of fluid separating walls where two fluids pass is 300μm, X-ray CT scanning is performed for HEX to observe defects and if there exist any holes to cause leakage. According to the X-ray CT scanning results, it appears no defects, holes, or voids between walls that will cause leakage or mixing of fluids. Thermo-hydraulic characteristics are evaluated by conducting experiments using water as operating fluid in the range of 100-270 milliliters per minute for flow rate. After experiments, the overall heat transfer coefficient of HEX is specified as 120-160 W/m^{2}K. Conjugate heat transfer finite element analysis is conducted with COMSOL Multiphysics and it is seen that additively manufactured HEX with gyroid lattice structure has an advantage over the conventionally manufactured HEX with a 55% increase in the effective-

ness and 90% decrease in its size. Klein et al. [28] stated that additively manufactured HEXs are studied and reviewed very briefly in terms of surface roughness, porosity, and feature thickness. For the effect of surface roughness in fluid channels of HEXs, more perceptible and quantitative information must be gained to predict heat transfer and flow characteristics well before manufacturing parts. As stated in the study, 5-35μm surface roughness values can be observed in SLS. Although increased surface roughness increases heat transfer area, it can decrease the thermal performance of the HEX with increasing pressure drop in the channel. Porosity, which is a common defect in AM, can be resulted from shrinkage, gas entrapment, etc., and can negatively affect thermal conductivity and structural properties of parts in the way of tensile and fatigue strength. In terms of feature thickness, smaller wall thickness leads to decreased overall thermal resistance and increased HEX effectiveness in which metal and polymer AM processes have 150μm and 32-100μm smallest feature thickness, respectively, as stated in the literature.

For additively manufactured cold plates; flow characteristics, thermal conductivity, pressure drop values, and temperature mapping are the main parameters to be inspected to compare theoretical values with practical test results and to measure the thermal performance [29]. For example, in the study of Caliskan et al. [30], card coolers with micro-channels are produced with AlSi10Mg by the DMLS method. Six different channel cross-section geometries called cylindrical, wide oval, drop form, hexagonal, narrow oval, and pentagonal, are used to produce card coolers considering supportless manufacturing. For manufactured parts, Micro-CT analysis is performed via a Nikon X TH device with 160 kV. CFD analysis is carried out with ANSYS Fluent software for the desired channel geometry which is designed in CAD software. For the channel model obtained after Micro-CT analysis, which includes deterioration in the manufacturing process, CFD analysis is conducted again. Due to the sagging problem, changes in hydraulic diameters, cross-section perimeters, and Reynolds numbers are observed. As a result, irregularities around the internal channel faces and sagging after the production of parts are affected the cooling rate and flow negatively. Elkholy et al. [31] studied the effect of fill ratio, layer height, and raster width of extruded material, which is pushed through an FFF printer nozzle, numerically and experimentally to distinguish the thermal conductivity of parts made via

3D printing. Anisotropic thermal properties of additively manufactured parts that are printed unidirectional are investigated and satisfying results are obtained to predict the thermal nature of HEXs.

For thermal applications such as cold plates, heat sinks, or HEXs, copper has advantageous properties in terms of thermal conductivity. Thus, many studies about AM of copper with differing methods for various applications have been carried out in the literature. For instance, Sciacca et al. [32] used Laser Powder Bed Fusion (LPBF) method to manufacture complex heat sinks with pure copper material. One helix type and two lattice type designs are used for heat sinks. These prototypes are modeled and analyzed both numerically and experimentally. Heat transfer coefficients and flow velocities are also considered and temperature mappings are compared between numerical analysis conducted in ANSYS and experimental results. The suitability of pure copper production via LPBF is shown in terms of manufacturing complex parts for liquid cooling and convenience in thermal performance prediction after CFD analyses. Manufacturing of copper parts with LPBF, EBM, Directed Energy Deposition (DED), Binder Jetting (BJ), ADAM, and Bound Metal Deposition (BMD) methods are discussed by Campagnoli et al. [33]. It is stated that high laser reflectivity with copper powders, ductile properties of copper which affects powder removal negatively and high thermal gradients between the melt pool and surrounding area which decreases the part quality are the main issues that can be faced during AM of copper. Process parameters are reviewed in detail according to the manufacturing methods. Properties of copper are compared between ADAM, BMD, and LPBF. Datasheet info on copper produced with ADAM and BMD is stated in terms of density, thermal conductivity, yield, and ultimate tensile strength. Singer et al. [34] presented various parts that are manufactured with copper. A concept pure copper HEX produced via DMLS and DMLS machine is modified before fabrication due to the reflectivity of copper. Tool inserts with internal cooling channels made from Hovadur K220 by SLM are presented. With using an SLM machine, a rocket combustion chamber is produced from GRCo-84 C Alloy to use in NASA projects. Cellular hollow copper structures are built with BJ processes to use both advantages of copper's thermal conductivity and the lower mass of cellular structures. A complex copper part that has internal cooling channels is produced via EBM with high purity. All these works

show that additively manufactured copper parts can be used in many areas, especially in thermal applications.

Micro-CT scanning of parts manufactured with AM is a crucial step to validate and control the quality of components. This method is used to check and evaluate the porosity of parts without damaging them. Singh et al. [35] performed Micro-CT evaluation by using an EasyTom XL device at 150 kV and 5.2μm voxel size. Relative densities are calculated with Archimedes method for the sintered parts and the highest relative density is obtained for the part sintered at 1050°C for three hours with 94.5%. After Micro-CT scanning, extrusion voids and printing voids are observed before sintering (green part). Porosity is also calculated as 4.1%, approximately, which is close to the value stated as 5.5% acquired from the relative density. In addition, the average equivalent diameter of pores is measured as 15μm for the sintered body according to the voxel resolution of 5.2μm. Three specimens made of novel CuCr1 powder printed with the LPBF method are scanned with Micro-Ct for defects, cavities, and porosity to determine building errors and to evaluate density in the study of Sinico et al. [36]. A high X-ray mass attenuation coefficient of copper is indicated which challenges CT scanning of copper specimens. Nikon XTH 225ST device is used for scanning with 195 kV. Since the resolution accuracy of CT scan is limited due to high laser source voltage, porosity results found within parts are less in Micro-CT analysis than porosity measured in Archimedes method. In the work of Thafarallah et al. [37], copper powders are mixed with NaCl, then compressed and sintered. After removing NaCl with warm water, a porous copper sample is obtained. Next, Micro-CT scanning is operated via Skyscan 1176 with 60 kV voltage and 35μm pixel size. To obtain the near-exact shape of porous geometry after scanning, different image enhancement techniques are used to eliminate noises on the tomogram, and reconstruction of volume with meshing is done with different software. As a result, the reconstruction of a porous copper structure is achieved appropriately. Jin et al. [38] crushed copper sulfide ore samples and scanned them by micro X-ray CT device, that is Zeiss Xradia 400 Micro X-ray CT, at an X-ray energy of 170 kV which shows the suitability of a potential sorting and selection method for ores. Mohd et al. [39] presented the effect of the filtering type on the quality of scanning. In the research, an aluminum engine bracket is scanned by using an industrial X-ray CT de-

vice performing at 135kV with four different filtering materials. Townsend et al. [40] extracted areal surface information of artifacts produced by an SLM machine using AlSi10Mg powder by scanning them using a Nikon XT H 225 Micro-Ct device. It is shown that results obtained with Micro-CT scanning and conventional optical surface texture measurement techniques are exceptionally alike with satisfying repeatability. Metrological X-ray CT scan is performed on Inconel 625 parts produced with LPBF system to investigate different internal features in the study of Kim et al. [41]. Nikon XT H 225 ST is used for Metrological X-ray CT at 180-200 kV for the parts that have cube and sphere internal features. Various internal features that are observed after the X-ray CT scan are compared with the CAD data and interior surfaces are placed to CAD geometry with a best-fit algorithm. Deviations from the nominal geometry are determined as a maximum of 0.1 mm and it is seen that decreasing interior feature dimensions results in increasing difference between produced geometry and the CAD model.

2.6 Closure

Complex parts having liquid channels and interior voids are hard to manufacture via traditional methods. However, AM turns into an alternative way to produce those kinds of products. As it is described in the literature review, there is a limited number of studies published relating to the end-use products fabricated via the M-FFF method. Thus, a study of cold plate fabrication via the M-FFF method and evaluation of them in terms of thermal performance is desired to be added to the literature. Therefore, different cold plates are fabricated with different cross-sections which are convenient to produce with supportless manufacturing in the M-FFF method. Since there are limited of works on the M-FFF process, the method's performance is evaluated with various characterization and quality control techniques for copper material in this study.

CHAPTER 3

PERFORMANCE EVALUATION OF THE METAL FUSED FILAMENT FABRICATION PROCESS

In this chapter, *design* and *fabrication* steps of the test parts are explained and demonstrated. Then *material characterization* of the raw material and *quality control* of the manufactured parts are investigated.

3.1 Design and Fabrication of Test Parts

Test parts replicating the cold plates are designed and manufactured using the M-FFF method to perform preliminary tests and measurements. Design and fabrication steps are explained in the following subsections.

3.1.1 Design

There are some parameters that affect the thermal performance and efficiency of a cold plate. Parameters such as material, channel type and size, cooling path, and fin location can be optimized and adjusted to increase the thermal performance of a cold plate. Cross-section of the channel affects the thermal performance of the cold plate proportionally according to its heat transfer area. However, the liquid's flow characteristics and the cold plate's manufacturability must be evaluated during the design process. Since support structures printed inside the part cannot be removed after fabrication, interior channels must be printed without support structures to obtain the desired flow. To produce the desired channel geometry, the design process must be performed according to the overhang angle criterion of the selected material.

For the proposed cold plate designs, copper is used for manufacturing with the M-FFF, which has advantageous thermal properties for thermal applications. Also, parts with pure copper material can be produced easier with M-FFF than SLM methods since the high reflectivity of copper powder is a problem in the laser sintering process. Because pure copper's overhang angle requirement is 50º, angles larger than 50º are chosen for supportless manufacturing of channels. As stated before, the thermal performance of different types of channel cross-sections is one of the critical points. Four different channel cross-sections are designed to control the quality of the test parts. 50º of overhang angle is considered during the design of these cross-sections. These cross sections are limited to an area with a 5.5 mm diameter which is a restricted dimension by quick couplings used in cold plate assembly. In the first cross-section, a droplet alike cross section (CS1) is designed, which is a typical shape for supportless manufacturing. A bigger flow area is formed in the second cross-section (CS2), which is like a triangle. In the third one, a column is constituted in the middle of the cross-section (CS3) to increase the heat transfer area. In the fourth cross section (CS4), two fin structures are added throughout the channel path. Fins are designed with 2.25 mm of height and 1 mm of width with 1 mm space between them. 1 mm width of the fin is chosen due to the requirement stated in the design guide of the Metal X 3D printer [42]. It is stated that, embosses less than 2.0 mm must be designed with a multiple of 0.25 mm to prevent gaps in features. Essential dimensions of the cross sections are remarked in Figure 3.1. Specified cross sections have different perimeters and areas (Table 3.1) which directly affect the heat transfer area of the cold plate since the same channel path is constructed for each cold plate.

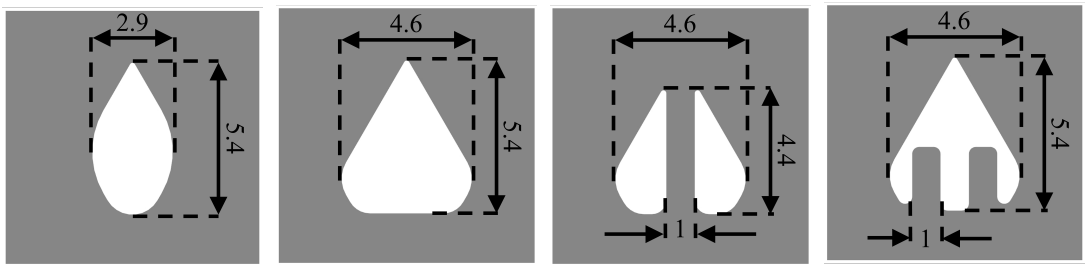

(a) CS1 - Droplet. (b) CS2 - Triangle. (c) CS3 - Column. (d) CS4 - Fin.

Figure 3.1: Dimensions of the cross-sections in mm.

Table 3.1: Perimeters and areas of the cross-sections.

Cross Section	Section Perimeter [mm]	Section Area [mm^2]
CS1	12.9	10.6
CS2	15.7	15.5
CS3	20.7	10.3
CS4	23.2	10.9

Two kinds of testing parts are designed to observe the manufacturability of the cross-sections. In the first testing part, the aim is to monitor the quality of the cross-section, supportless manufacturing results, and uniformity of sintered part over a straight channel (Figure 3.2). In the second part, the same parameters are utilized for the angled channels (Figure 3.3). Also, a cylinder part is designed with 10 mm in diameter and 10 mm in height to determine the density and porosity parameters of copper.

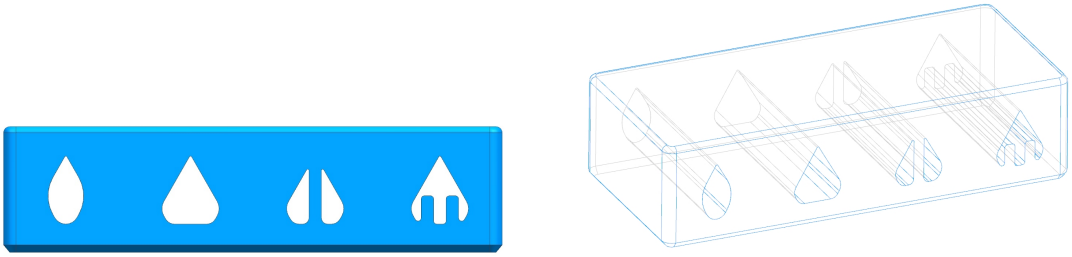

(a) Front view of straight test part design.

(b) Wire frame of straight test part design.

Figure 3.2: Straight channel test part design

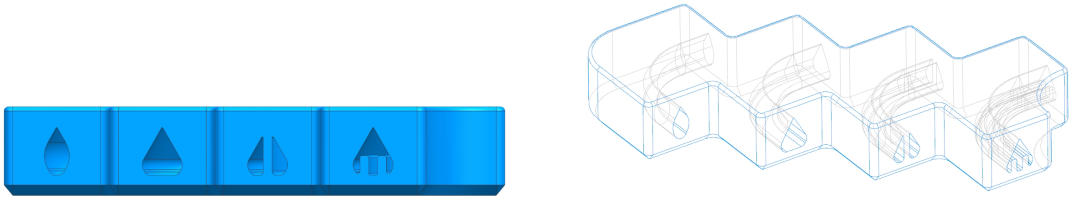

(a) Front view of the angled test part.

(b) Wire frame of the angled test part.

Figure 3.3: Angled test part.

Outer regions of the parts don't include sharp corners like channel cross-sections. Radii are formed to eliminate sharp corners and residual stress that shows up during sintering and to conserve the uniformity of the part. To separate the part from the printing bed easily and without damage, a 50º chamfer with a 1 mm width is generated on the lowest edges of the part, which is a recommended method for parts manufactured with the ADAM method. After the design process, CAD parts in .stl format are uploaded to the CAM software of Markforged company, which is an online CAM software, to adjust the printing settings of the parts before sending them to a printer. In the CAM software, material, printer, sintering furnace, printing orientation, and the number of wall contours are chosen first. After setting these parameters, printing details of the part such as printed and sintered dimensions and masses; print, wash and dry times; material costs, slicing, layers, and nozzle path, are specified. Printing simulations of the straight and the angled test parts made of copper are demonstrated in the CAM software before fabrication (Figure 3.4). Part details related to printing are noted in Table 3.2.

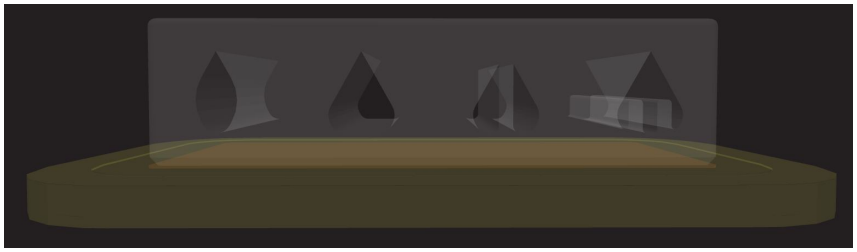

(a) Printing simulation of the straight channel test part.

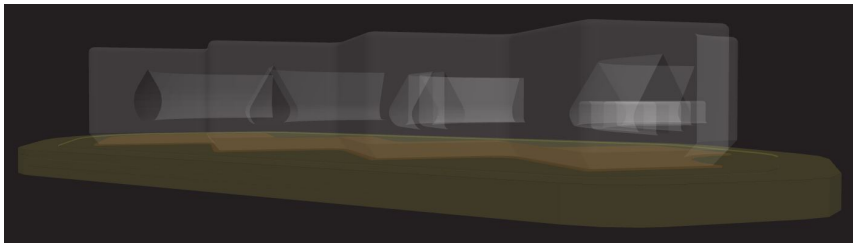

(b) Printing simulation of the angled channel test part.

Figure 3.4: Support control and layer view in the CAM software. Yellow is the raft, orange is the ceramic release and white is the part.

Table 3.2: Printing details of the test parts in the CAM software.

Test parts	Straight	Angled	Cylinder
Printed dimensions [mm]	46.4×20.9×11.9	66.2×66.2×11.9	⌀11.6×11.9
Final part dimensions [mm]	40×18×10	57×57×10	⌀10×10
Print time [hour]	7.2	13.2	2.5
Wash time [hour]	12.5	31	20
Dry time [hour]	4		
Printed part mass [g]	89.6	178.2	16.3
Final part mass [g]	53.7	111	6.5
Material cost [USD]	21.9	43.6	4.0
Number of walls	4		

3.1.2 Fabrication

The straight and the angled interior channels are fabricated separately to investigate the characteristics of supportless manufacturing and observe sagging or warping effects on the liquid channel faces. The fabrication is completed using the Metal X 3D printer (Figure 3.5a) of the Markforged company. The Metal X 3D Printer uses the ADAM method, which has a build volume of 300×220×180 mm. The printer has two nozzles, for metal material extrusion and ceramic support release material extrusion. It has two resolution options, 50 and 200 μm. After the fabrication on the 3D printer, green parts, which include both plastic and metal materials inside, are acquired (Figure 3.6). Green parts are subjected to a washing process in the Wash-1 device of the Markforged to remove binders and clean parts, which results in obtaining brown parts. Then the sintering process is employed on the brown parts for 29 hours to remove all plastic and binder materials and bond metal powders together in the Sinter-2 furnace of Markforged which can rise the temperature of the chamber up to 1300°C (Figure 3.5b). During the sintering process, parts shrunk due to the plastic and binder removal. Printed part dimensions shrink 14% on x- and y-axis and 16% on z-axis for copper material in the M-FFF process. Therefore, parts are printed larger

than the desired dimensions according to the shrinkage values.

(a) The Metal X 3D printer.

(b) The Sinter-2 furnace.

Figure 3.5: Equipment used in M-FFF.

While printing the test parts, 200 μm resolution is used. Test parts are made of 17-4 PH SS and copper. Since only 17-4 PH SS was initially available in the company, a straight test part is manufactured with 17-4 PH SS (Figure 3.7) to control the convenience of support generation on the CAM software. Then, the straight (Figure 3.8a) and the angled (Figure 3.8b) test parts are produced with copper material which is aimed to be used in the proposed cold plates due to its thermal conductivity which is an ideal property for thermal applications. The cylinder part used in some of the characterization tests is shown in Figure 3.9.

3.2 Material Characterization and Quality Control

Manufactured test parts using the M-FFF method, are subjected to preliminary material characterization and quality control tests such as measurement of *surface roughness*, determination of dimensional accuracy with the *CMM*, scanning of parts with

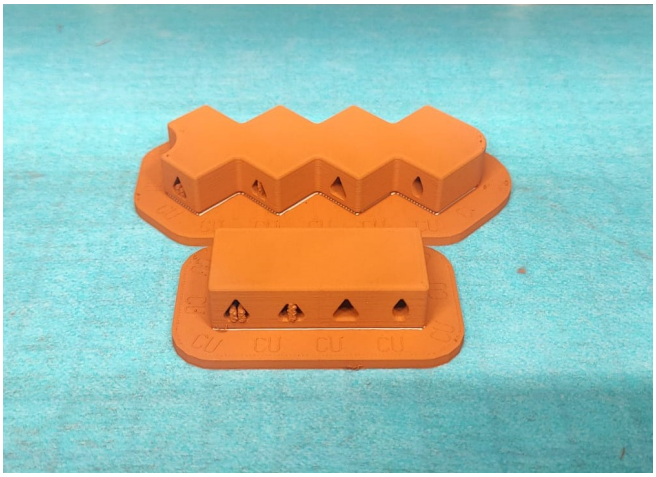

Figure 3.6: Green state of manufactured straight and angled test parts.

Figure 3.7: Straight test part made of 17-4 PH SS.

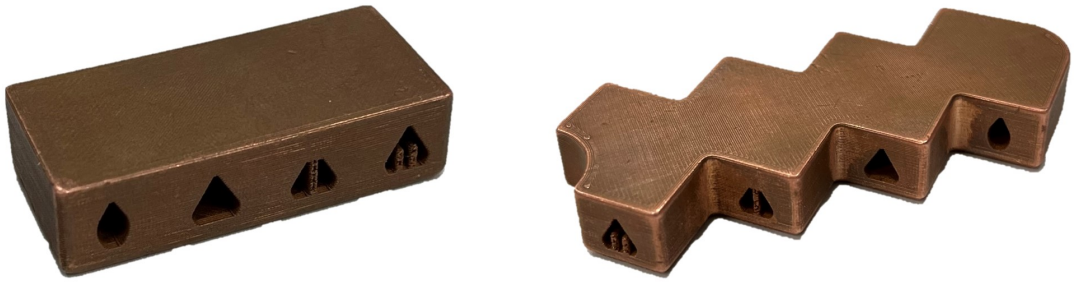

(a) Straight test part made of copper.

(b) Angled test part made of copper.

Figure 3.8: Test parts made of copper.

the *Micro-CT* device, calculating the density of material with the *Archimedes method*, determination of porosity within the part with *SEM analysis* and estimation of the *thermal conductivity*.

Before material characterization and quality control tests, the test parts are inspected visually. High surface roughness at the bottom face of the test parts is observed due to

Figure 3.9: Cylinder part made of copper.

the ceramic layer between the raft and the metal part. Deteriorations due to sagging and spoilt extrusions are observed in the column structure of CS3 and the fin structure of CS4. The interior faces of the straight and angled test parts are less rougher than the internal faces of the channels manufactured with the SLM method.

Measured masses of the test parts and the mass values calculated in the CAD software are stated in Table 3.3.

Table 3.3: Masses of the test parts.

Test Part	**Material**	**Mass in CAD [g]**	**Actual Mass [g]**	**Difference**
Straight	17-4 PH SS	48.9	43.0	-12.1%
Straight	Copper	53.7	54.3	+1.1%
Angled	Copper	111	112.8	+1.6%
Cylinder	Copper	6.5	6.7	+3.1%

3.2.1 CMM

Dimensions of the straight and the angled test parts are measured with the Delta Slant gantry type CMM of Hexagon (Figure 3.10). Mainly, the outer dimensions of the test parts are measured with the CMM, such as width, length, and height. For CS1 and CS2, channel height and width are measured with CMM as appropriately as possible. For CS3 and CS4, the CMM probe couldn't touch the faces of the interior channel

since the probe diameter is 0.8 mm and the probe is bent while touching the interior faces. In addition, because of the deterioration of the column and the fin structures of CS3 and CS4, the risk of breaking the probe is increased. Thus, a microscope and a digital caliper are used for the measurement of these dimensions.

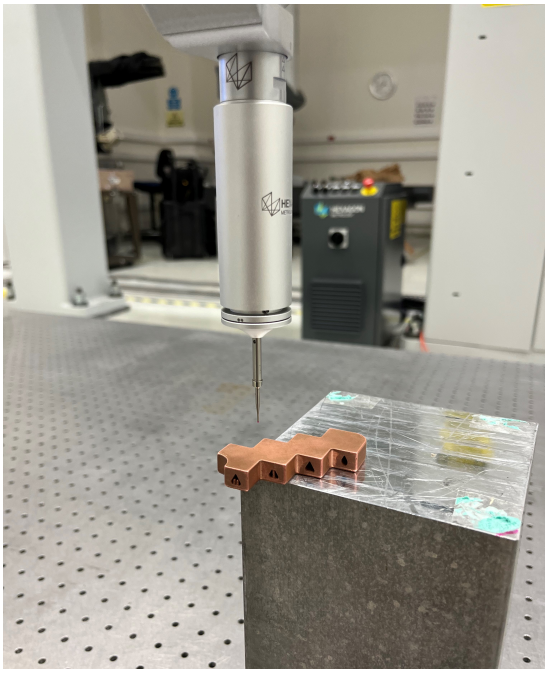

Figure 3.10: CMM measurements of the test parts.

Outer dimensions of the test parts are shown in Table 3.4. When the results are elaborated, it is seen that 17-4 PH SS part has more deviation than the copper counterparts in x- and y-axis, which are length and width, respectively. But in z-axis, 17-4 PH SS has a better result. Similar deviations are observed when the outer dimensions of the copper test parts are compared. For all outer dimensions in all axes of the three test parts, actual dimensions are greater than the nominal values, and much higher tolerances are obtained compared to the tolerances in the traditional manufacturing methods.

The results of the essential dimensions of channel cross-sections of copper test parts are shown in Table 3.5. Similar results are obtained when the straight and the angled copper test parts are compared. Dimensions for the channel height are less than the nominal dimensions. Fin thicknesses are mostly greater than the nominal dimensions, but there are some deteriorations in the fin thicknesses of both structures (Figure

Table 3.4: Outer dimensions of the test parts.

	Part	Straight	Straight	Angled
	Material	17-4 PH SS	Copper	Copper
Width [mm]	**CAD Dimension**	18	18	57
	Actual Dimension	18.43	18.14	57.16
	Deviation	+0.43	+0.14	+0.16
Length [mm]	**CAD Dimension**	40	40	57
	Actual Dimension	40.57	40.27	57.11
	Deviation	+0.57	+0.27	+0.11
Height [mm]	**CAD Dimension**	10	10	10
	Actual Dimension	10.09	10.29	10.24
	Deviation	+0.09	+0.29	+0.24

3.11 and Figure 3.12). These deteriorations affected average fin thickness negatively. 0.82 mm and 1.32 mm of fin thicknesses are observed when the lower and the upper limits are considered, which can be originated from spoilt extrusion, sagging, and uncontrolled shrinkage.

(a) Front view.

(b) Back view.

Figure 3.11: Deteriorations on the fin structures of CS3 and CS4 of the straight test parts.

CMM measurements of the cylinder test parts are shown in Table 3.6. The height of the cylinder is measured to be more than the nominal dimension. The actual diameter of the cylinder is 9.9 mm, with a 0.1 mm deviation from the designed value, which is acceptable when compared with traditional machining methods.

Table 3.5: Dimensions of the channel cross-sections of copper test parts.

	Part	Straight	Angled
CS1 Height [mm]	**CAD Dimension**	5.5	5.5
	Actual Dimension	5.34	5.35
	Deviation	-0.16	-0.15
CS2 Height [mm]	**CAD Dimension**	5.5	5.5
	Actual Dimension	5.36	5.33
	Deviation	-0.14	-0.17
CS3 Height [mm]	**CAD Dimension**	4.63	4.63
	Actual Dimension	4.18	4.11
	Deviation	-0.45	-0.52
CS3 Fin Thickness [mm]	**CAD Dimension**	1	1
	Actual Dimension	1.25	1.07
	Deviation	+0.25	+0.07
CS4 Height [mm]	**CAD Dimension**	5.5	5.5
	Actual Dimension	5.36	5.37
	Deviation	-0.14	-0.13
CS4 Fin Thickness [mm]	**CAD Dimension**	1	1
	Actual Dimension	0.99	1.05
	Deviation	-0.01	+0.05

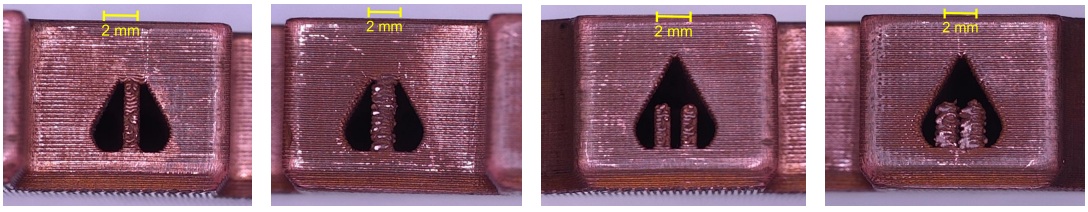

(a) Start of CS3. (b) End of CS3. (c) Start of CS4. (d) End of CS4.

Figure 3.12: Deterioration on the fin structures of CS3 and CS4 of angled test part.

Table 3.6: Dimensions of the copper cylinder test parts.

Diameter [mm]	**Nominal Dimension**	10
	Actual Dimension	9.9
	Deviation	-0.1
Height [mm]	**Nominal Dimension**	10
	Actual Dimension	10.34
	Deviation	+0.34

3.2.2 Surface Roughness

Surface roughness is a surface property that determines the surface quality of a part. Summation of deviations in the normal vector of the surface expresses surface roughness. Surface roughness affects the appropriateness of assembly, friction, and wear on the surface. Ra value indicates an arithmetic average of height deviation from the mean profile of the surface, and Rz value indicates the distance between the upper and the lower points on the surface that is investigated.

Surface roughness of the test parts is measured by the Mitutoyo Surftest SJ-400 device (Figure 3.13). Ra and Rz values are measured for upper surface, side surface, and bottom surface of the copper test parts and are indicated in Table 3.7.

Table 3.7: Surface roughness of the copper test parts.

	Top Surface		**Side Surface**		**Bottom Surface**	
Part	**Ra [μm]**	**Rz [μm]**	**Ra [μm]**	**Rz [μm]**	**Ra [μm]**	**Rz [μm]**
Straight	1.95	12.01	6.07	31.65	26.02	105.3
Angled	1.33	8.3	12.33	51.5	32.79	129.2

As seen from Ra and Rz values of the straight and the angled copper test parts, results are similar to each other. When surfaces are compared, the best surface quality is obtained on the upper surface, which is close to the surface roughness values of machined parts. Regarding the side surface, Ra and Rz values are fairly average and

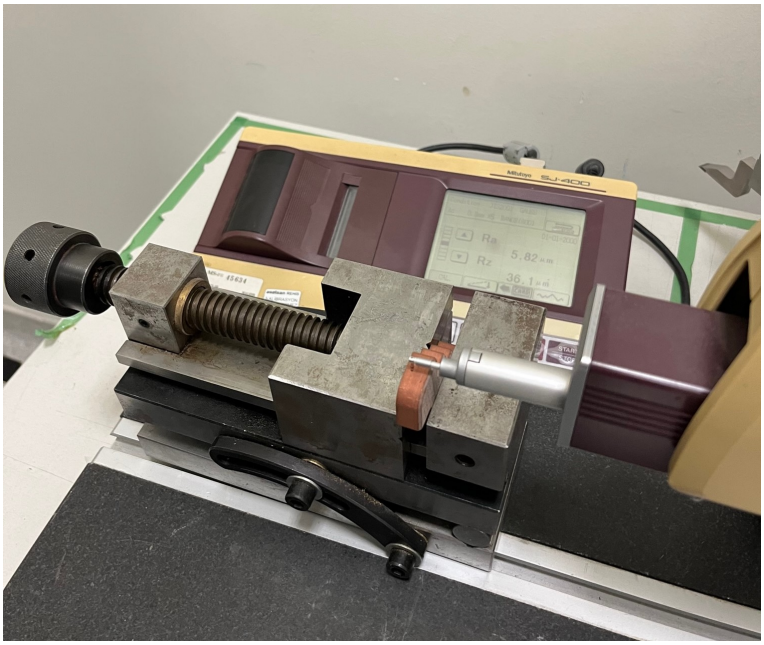

Figure 3.13: Surface roughness measurement.

increased compared to the upper surface since the staircase effect is more perceivable. But on the bottom surface, surface roughness is increased significantly due to the ceramic layer residuals, which separates the final part and raft during production. Due to the sintering of the part, the ceramic layer becomes more powdery and spoils the quality of the bottom surface of the final part. For the surface roughness on the faces of interior channels, obtained results are between the upper surface and side surface results. Some sections of the test parts are cut, and surface roughness is measured for the interior channel sections. Since the interior faces of the channels both have flat surfaces and side surfaces with staircase effects, various Ra and Rz values are collected. Precise results couldn't be given for the stated faces, therefore noticed limits are specified.

3.2.3 Archimedes Method

Undesired porosity throughout the parts decreases the strength of the material and can cause crack propagation after force is applied. Also, density must be specified for the unknown materials to calculate other material properties and obtain the mass. To gain insight into the porosity and density of parts, Archimedes method, a measurement

procedure to determine the density of parts, is applied for copper cylinder test parts (Figure 3.9). This method is based on measuring the test part's weight in air and water where the part is fully submerged. This difference gives the buoyancy force, which equals the weight of the displaced fluid. Since the part is completely submerged and the volume is the same for both cases, the ratio of the density of the test part and the density of the fluid equals to the ratio of the weight of the test part and the weight of the displaced fluid. As built parts are used, which means no machining or grinding operation is applied on the cylinder specimens. Density is evaluated according to the ISO 3369 test standard. Archimedes method is performed by using the Precis XB 220A device at 24°C ambient temperature (Figure 3.14). Measured densities of copper specimens are calculated via the following equation

$$\rho = (\frac{m_a}{m_a - m_w})\rho_w \tag{3.1}$$

where m_a is the mass of the test piece determined by weighing in air, m_w is the mass of the test part in liquid, and ρ_w is the density of distilled water at 24°C ambient temperature which equals to 0.9973 g/cm^3 as specified in the standard. After the specimens are laid on the attachment in the water side of the device, no significant air bubbles are observed on the outer surfaces of them.

After measuring the masses of the test parts in air and water, respectively, density values are obtained according to the previously stated Equation 3.1. The average density value for the test parts is found as 8.6462 g/cm^3 where the standard deviation is 0.0383. Relative density is calculated as 96.50%, where Markforged specifies [43] it as 98% in the datasheet for copper used on the 3D printer. That means copper specimens have 3.50% porosity inside on average. Defects in the part, such as open pores or closed pores infilled with air or bubbles, may be the major reasons for the difference in relative density, which increases the porosity level of the parts.

3.2.4 SEM Analysis

Optic Microscope and SEM are used to analyze the porosity of the copper parts after sectioning. Manufactured copper cylinder parts are used for sectioning; speci-

Figure 3.14: Determination of density with the Archimedes method.

mens are machined by a lathe and ground with 800-grit sandpaper to obtain a surface as smooth as possible (Figure 3.15). First, specimens are examined with a Nikon Eclypse MA200 optic microscope. The quality of section images is obtained insufficiently which can be seen in Figure 3.16. Grinding marks are dominant in observation and it is not possible to separate marks and voids. Therefore, images obtained from an optic microscope are not used to evaluate porosity.

Figure 3.15: After machining and grinding of the cylinder test part.

Then, the Phenom XL G2 SEM is used to observe sections of the parts in a more detailed manner. Randomly distributed voids are detected during screening. Although

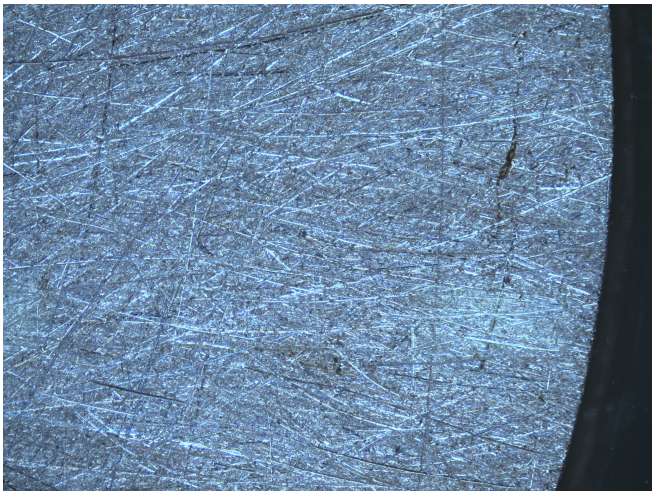

Figure 3.16: Section observation of copper part with an optic microscope.

grinding marks are dominant again, porous structures are obtained more separable throughout the section. As mentioned before, there is no significant distribution of voids on the sectioned surface according to the occurrence in some specific areas, such as around the peripheral or close to the center. Screening images show that voids are distributed randomly around the sectioned surface. Some images obtained with 265x zoom using the SEM are demonstrated in Figure 3.17 where example larger pore areas are marked.

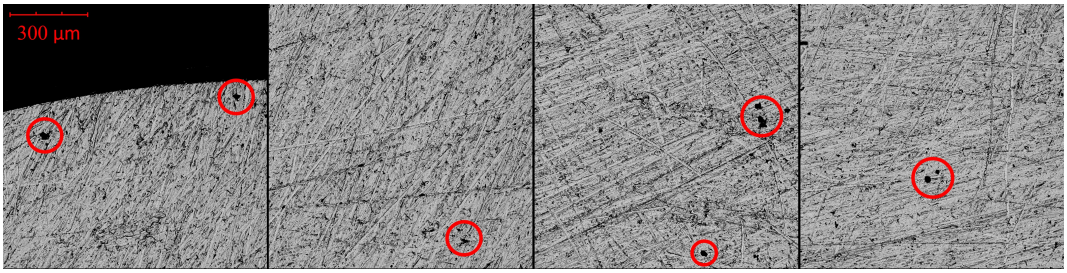

Figure 3.17: Some SEM images of the cylinder test parts, red circles indicate example larger pore areas.

Images are subjected to image processing on ImageJ software to perform porosity analysis. 3.92% of porosity is obtained, close to the result obtained in the Archimedes method. Relative density is calculated as 96.08%, which corresponds to the copper density of 8.6088 g/cm^3. The average area of the pores is 18.08 μm^2, which corresponds to an average diameter of 4.8 μm. Areas of pores less than 4 μm^2 are filtered

in ImageJ to eliminate grinding marks. The minimum and the maximum pore areas are calculated as 4.013 μm^2 and 944 μm^2, respectively. The distribution of commonly observed pore areas is demonstrated in Figure 3.18.

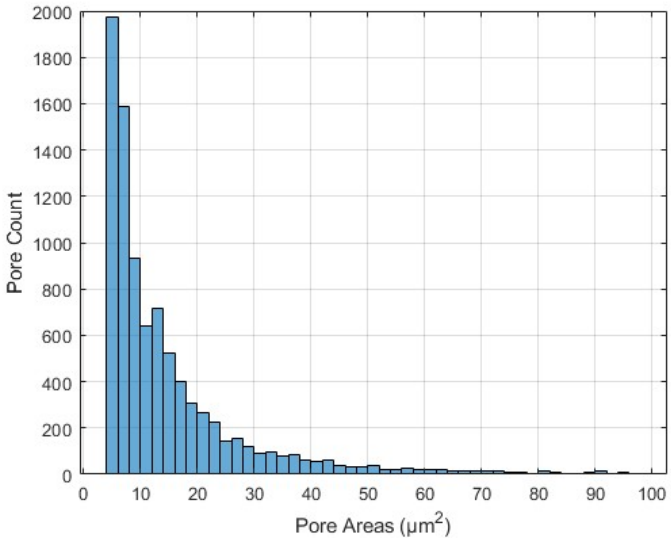

Figure 3.18: Histogram of pore areas.

3.2.5 Thermal Conductivity

Thermal conductivity is measured with the laser flash method (Figure 3.19a). Netzsch LFA 467 HT HyperFlash instrument is used for contactless measurement of thermal conductivity according to the ASTM E1461. A specimen with 15×15×5 mm outer dimensions is produced by using the ADAM method with copper material. Then, the specimen is machined to 10×10×2 mm dimensions which are necessary part dimensions to be used in thermal conductivity measurement (Figure 3.19b). The specimen is coated with graphite to prevent reflectivity on the part during measurement. It is placed in a sample holder and an integrated Xenon flash system is generated a short energy pulse at the front side of the specimen. Then, an infrared detector received the temperature rise on the rear side of the specimen as a function of time. Thermal diffusivity (a) is determined according to the parker-formula

$$a = 0.1388(\frac{l^2}{t_{1/2}}) \tag{3.2}$$

where a is the thermal diffusivity in mm^2/s, l is the thickness of the test piece in mm, and $t_{1/2}$ is the time at 50% of the temperature increase measured at the rear of the test piece in s. The specific heat is assumed as 0.385 J/gK which is stated in the copper material datasheet of the Markforged [43]. Then, the thermal conductivity is calculated for room temperature (25°C) according to the following equation.

$$\lambda(T) = a(T)\rho(T)c_{\mathrm{p}}(T) \tag{3.3}$$

where T is the selected temperature for measurements, λ is the thermal conductivity, a is the thermal diffusivity, ρ is the bulk density and c_p is the specific heat for the copper material. Thermal diffusivity is calculated via Equation 3.2 and bulk density is found 8.6462 g/cm^3 as stated in the Archimedes Method part. According to these values, thermal conductivity is calculated as 389.462 W/mK. Thermal conductivity is specified as 350 W/mK in the copper material datasheet of Markforged [43], where an 11.28% difference is obtained.

Porosities observed in the part can be the reason for the difference between the test result and the datasheet value. The accuracy of the outer dimensions of the specimen may be out of tolerance, therefore short energy pulse may affect detectors. Also, defects on the part due to the graphite coating may cause reflection that could affect results.

3.2.6 X-Ray and Micro-CT Scanning

X-ray imaging is performed to investigate the interior quality of the channel sections by taking images of the parts. X-ray inspection is done by using the Nordson Dage Quadra 7 instrument with an X-ray power of 160 kV. Details of the channel sections are illustrated in Figure 3.20. Since the test parts subjected to the X-ray scans are made of copper, details of the channel sections are obtained coarsely in observation because of the high density of copper. As a result of the changing areas of the cross sections, a blurry view around the channel occurs. The column structure of CS3 and the fin structure of CS4 is observed more precisely due to the constant and straight sections.

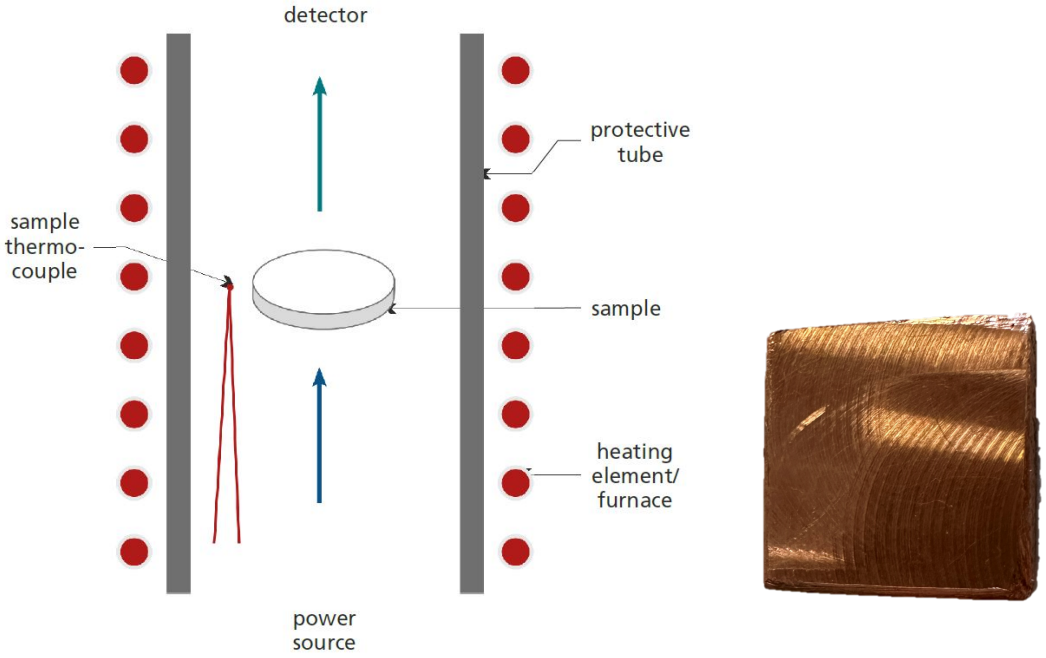

(a) Schematic of the flash method adapted from [44].

(b) The specimen.

Figure 3.19: Thermal conductivity measurements.

Then, the cylinder test part is subjected to X-ray Micro-CT scanning. Micro-CT scans are performed on the EasyTom CT microfocus system of RX Solutions. Scans are conducted at 225 kV of X-ray source which is an appropriate value for high-density parts such as copper. Voxel size is specified as 10μm, which is the minimum value of filtering for the scan resolution. According to the results obtained with the Micro-CT scans, 5.16% porosity is detected in the cylinder test part. Relative density is calculated as 94.84%, which corresponds to the copper density of 8.4978 g/cm^3. The density of the test part appeared to be lower after the Micro-CT analysis. X-ray noises that occurred during scans and different materials inside the test part that couldn't be eliminated with filtering are some reasons of high porosity. Considering the CT images (Figure 3.21) obtained after the scan, the porous structure of the test part is seen clearly. Pores between layers and between wall contours are differentiated evidently.

Repetition of pores at each layer and the same locations is observable from the CT images. Because of that, nozzle paths are investigated in the CAM software in detail.

(a) X-ray inspection of the straight test part.

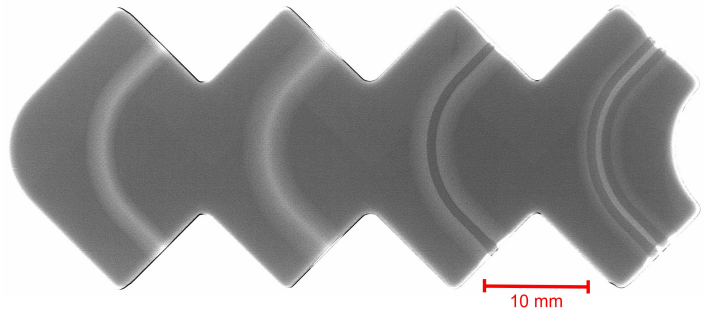

(b) X-ray inspection of the angled test part.

Figure 3.20: Copper test parts subjected to the X-ray scan.

The nozzle path turns 90° in every layer of the cylinder test part for solid filling, and the start-stop locations of the nozzle are the reason for the repetition of pores which can be seen in Figure 3.22. Discontinuity of path and problems in the overlapping of the extruded material increased the probability of porosity observation. Because of the filling path of the algorithm, possible porosity locations can arise within the parts at the start-stop locations of the nozzle in the M-FFF process. To eliminate this problem, the path algorithm must be updated to 67° turning at each layer, which is a common approach in various AM applications.

3.3 Closure

In Chapter 3, the performance of the M-FFF method is evaluated. Design and fabrication steps are investigated and discussed. Material characterization and quality

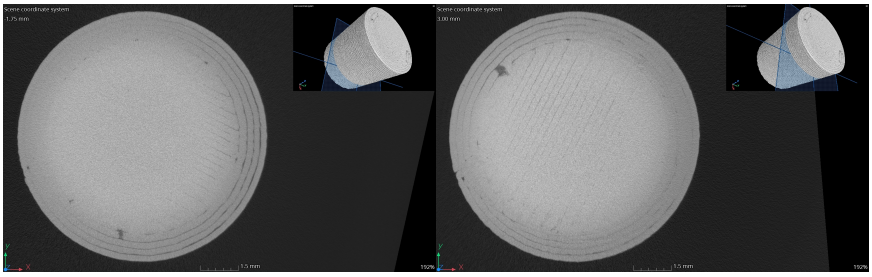

(a) Some sections from the top view of the cylinder test part.

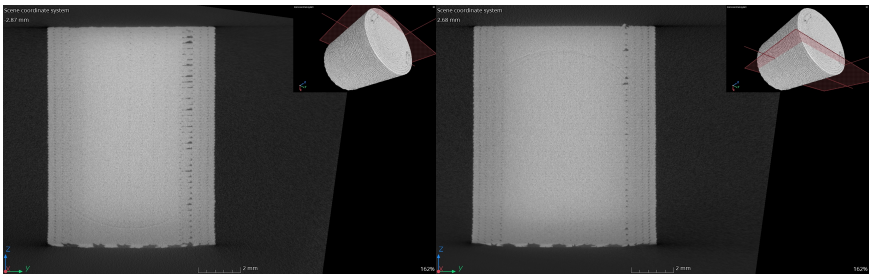

(b) Some sections from the right view of the cylinder test part.

Figure 3.21: Some examples of the section images obtained from the Micro-CT scan.

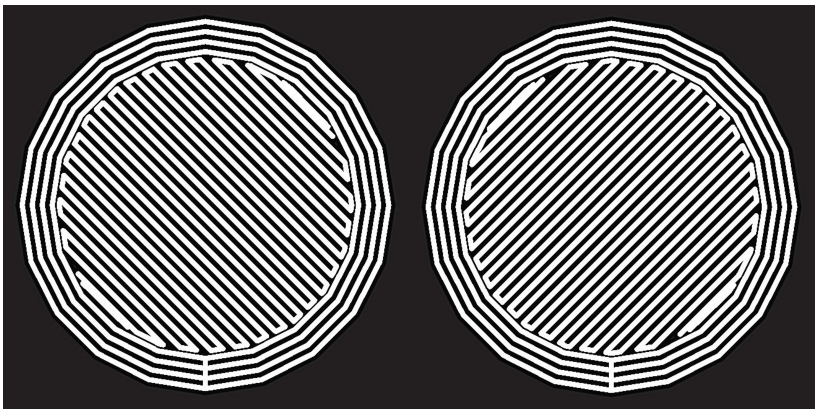

Figure 3.22: Nozzle path on the consecutive layers.

control tests are performed. It is observed that the M-FFF process can be used to manufacture the proposed cold plate designs. Manufacturing and evaluation of the cold plates are stated in the following section, Chapter 4.

CHAPTER 4

MANUFACTURING AND EVALUATION OF COLD PLATES

In this chapter, *design* and *fabrication* steps of the cold plates are explained and demonstrated. Afterward, manufactured cold plates are subjected to some *experimental tests*. Results of the experiments for the cold plates are explained in detail in terms of thermal performance. Then, *temperature mapping* of the cold plates is evaluated using a heat source, thermocouples, and a thermal camera.

4.1 Design and Fabrication of Cold Plates

All the previous test parts were fabricated and evaluated to design the cold plates in a better way. Points to consider for the design and fabrication of the cold plates are observed in the previous chapter. Designs of the cold plates are developed after material characterization and quality control of the test parts stated in Chapter 3. These designs are fabricated using the Metal-FFF method. Design and fabrication steps are explained in the following subsections.

4.1.1 Design

Four different cold plates are designed with four different cross sections which were investigated before. For the initial design step, horizontal liquid inlet and outlet orientation are used for the design of the cold plates. Since the utmost diameter of the quick coupling is larger than the thickness of the part of a cold plate where liquid circulates, the channel level must be raised (Figure 4.1a). This kind of design ends up with more metal material or more support structure (Figure 4.1b) which increases the

cost and time of production. Therefore, vertical liquid inlet and outlet orientation are used for the design of the cold plates.

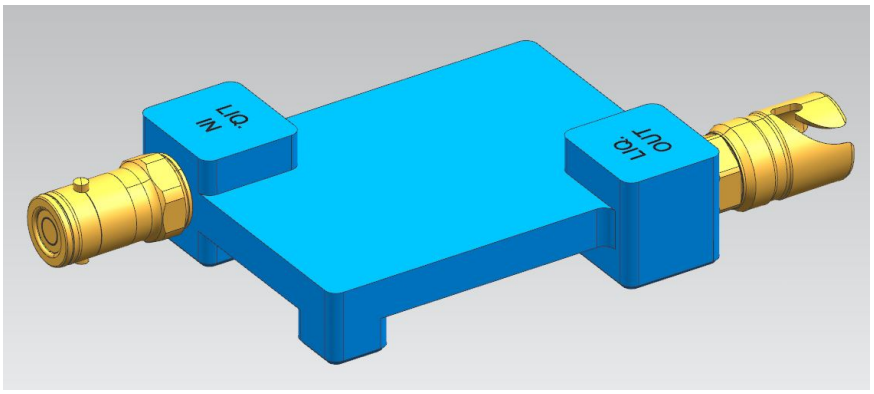

(a) Cold plate with raised channel level.

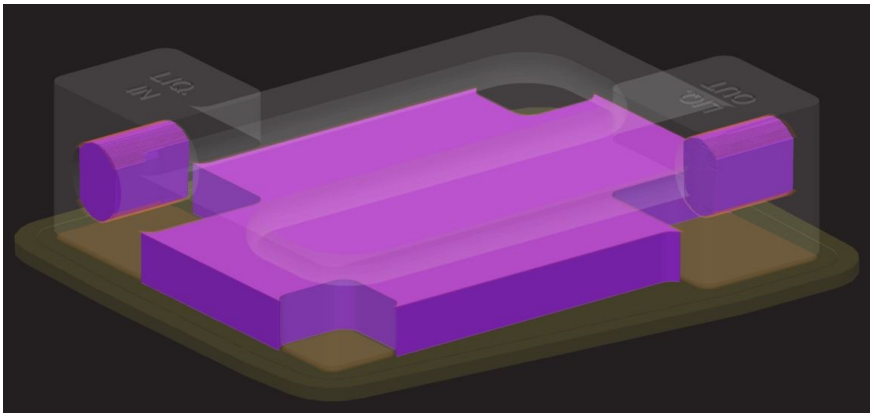

(b) Printing simulation of the initial cold plate design.

Figure 4.1: Initial cold plate design.

Then, vertical liquid inlet and outlet orientation are implemented in the new cold plate designs. Cold plate thickness, where the horizontal liquid channel is located, is set to 10 mm thickness. When this design is manufactured, a leakage problem is observed on the lower surface of the cold plate. A crack as a line under the middle part of the channel is the reason of this leakage. Manufactured cold plate is cut from various sections to investigate the crack observed under the liquid channel. Wire-Electrical Discharge Machining (W-EDM) method is used for cutting. The cold plate is placed inside a distilled water pool and cutting is performed with a brass wire with a diameter of 0.3 mm on a Sodick Premium AQ750L machine. Channel sections are investigated with a microscope after cutting, and the crack is observed more clearly (Figure 4.2).

In Figure 4.2a, crack line under the channel part located on the middle of the cold plate, is seen along the cold plate. Observed crack under the channel cross section and propagation of it throughout the channel can be seen in Figure 4.2b and Figure 4.2c, respectively. Problems occurred during debinding and sintering steps such as suspension of excessive plastic material or inhomogeneous temperature distribution may caused the fracture on the lower surface of the cold plate.

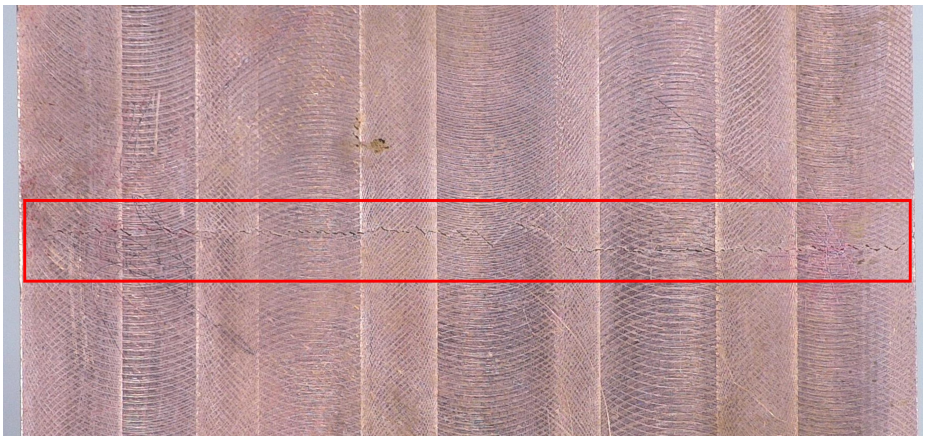

(a) Crack line on the lower surface of the cold plate.

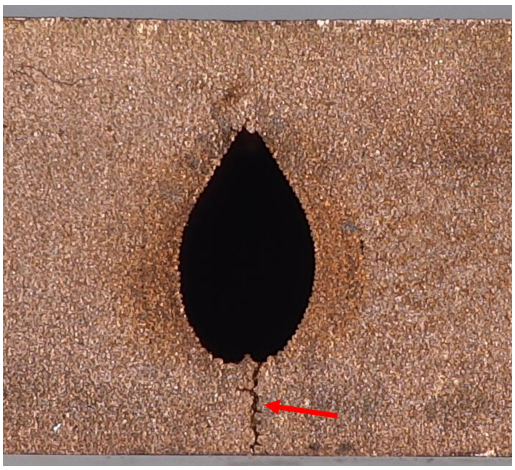

(b) Crack under the droplet channel.

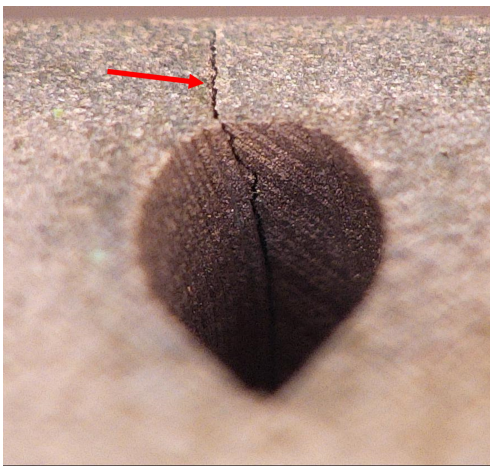

(c) Crack propagation through the channel.

Figure 4.2: Cracks observed on the cold plate after cutting.

The final design of the cold plate is demonstrated in Figure 4.3a which is designed in Siemens NX CAD software. Outer dimensions, chamfers, radii, and hole details are kept the same to leave the cross-sections as the only variable in the design. Vertical liquid inlet and outlet orientation are used for cold plates. For all the cold plates, the

liquid channel path (Figure 4.3b), which has two U-turns, is kept the same to compare the thermal performance of the cold plates in terms of different cross-sections. Since the liquid path is the same for all the designs, each channel cross-section has a different heat transfer area for liquid cooling. Also, different pressure drop values are expected throughout the channel because of different cross sections.

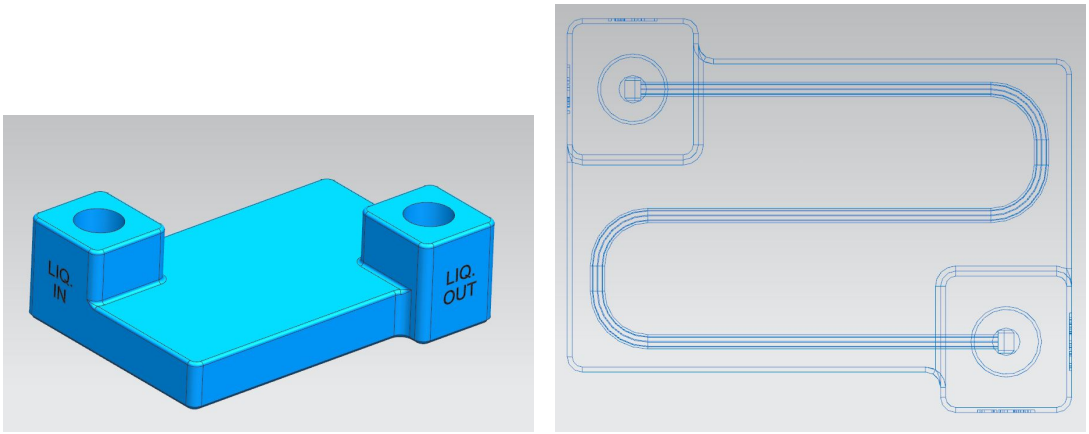

(a) The final cold plate design.

(b) Top view of the liquid channel path of a cold plate.

Figure 4.3: The final cold plate design.

Cold plate designs are named as CP1, CP2, CP3, and CP4 which include cross sections called CS1, CS2, CS3, and CS4, respectively. For all the cold plates, 1-3 mm radii are added for outer sharp edges to minimize residual stresses during the sintering process. As mentioned in the previous chapter, a 50º chamfer of 1 mm is generated on the lowest edges of the cold plates for easy separation of from the raft after sintering.

Liquid inlet and liquid outlet parts of the channel are indicated on the cold plates with "LIQ. IN" and "LIQ. OUT" texts. Texture details are added to the model according to the design reference set of The Metal X 3D printer. 4 mm height and 0.5 mm depth are used for letters engraved on the vertical surfaces.

Liquid flow passes through the cold plates by using hoses that have quick couplings at both ends. The transition of liquid is provided from liquid inlet and outlet areas of the cold plate with quick couplings which are the male and female couple of SPH08 model of Staubli. Assembly of the quick couplings and the cold plate can be seen in

Figure 4.4.

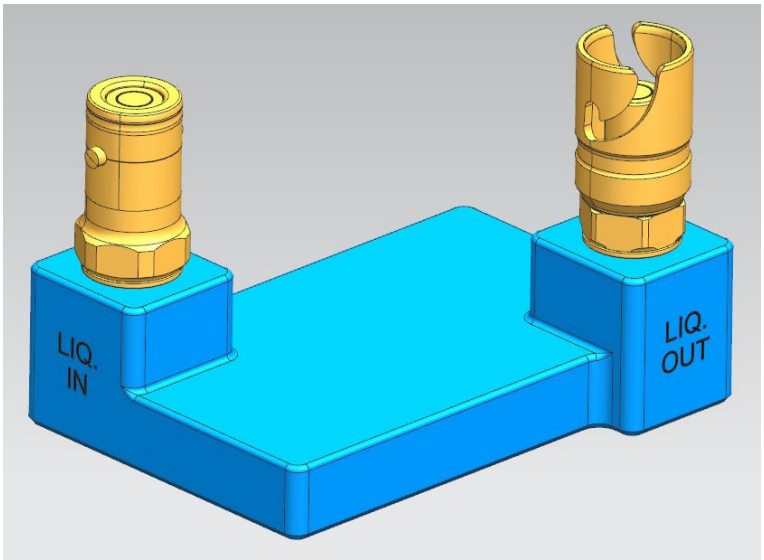

Figure 4.4: Quick couplings and cold plate assembly.

Stated quick couplings have G3/8 thread size which is a British Standard Pipe Parallel Thread and the assembly interface in the cold plate must be compatible with the quick couplings. G3/8 thread has a major diameter of 16.662 mm and a tap drill diameter of 15.0 mm. Therefore, liquid inlet and outlet holes are designed as 14.0 mm in the cold plates to enlarge them after manufacturing. Other details of inlet and outlet holes are designed according to the quick coupling dimensions and kept the same for all the cold plate designs.

After finishing the design of the cold plates, CAD geometries are exported in .stl format and uploaded to the CAM software to adjust the printing settings of the parts before fabrication. Printing simulation and internal view of a cold plate are demonstrated in Figure 4.5. Channels inside the cold plates have two U-turns, therefore parts to be manufactured are located horizontally in the print simulation not to have support structures interior. There would be support structures inside of the channel if the cold plates are located vertically or angled since the channels are circulating all around the plates. Part details related to the printing of four different cold plates are indicated in Table 4.1.

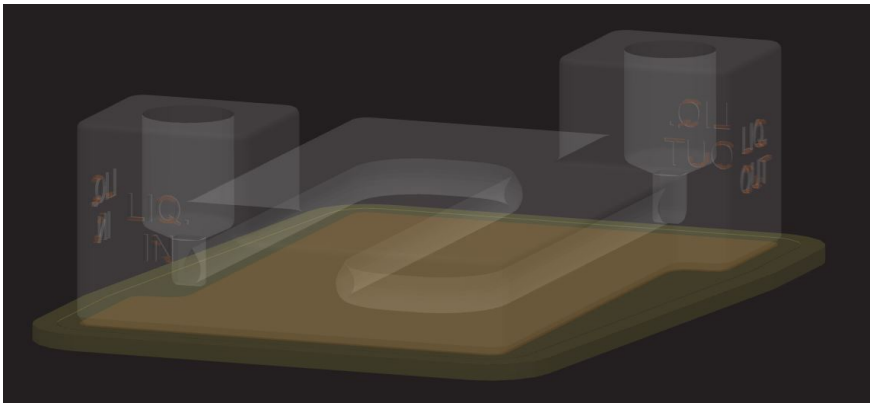

Figure 4.5: Printing simulation of the cold plate CP1.

Table 4.1: Printing details of copper cold plates in the CAM software.

Cold Plates	CP1	CP2	CP3	CP4
Printed dimensions [mm]	90.5×116.1×36.2			
Final part dimensions [mm]	78.0×100.0×30.5			
Print time [hour]	80	79	80	80
Wash time [hour]	50	45	45	45
Dry time [hour]	5	4.5	4.5	4.5
Printed part mass [g]	1190	1180	1190	1190
Final part mass [g]	936.6	924.9	936.7	935.0
Material cost [USD]	292.5	289.6	292.5	292.3
Number of walls	4			

4.1.2 Fabrication

The fabrication of the cold plates is done using the ADAM method with The Metal X 3D printer. 200 μm resolution is used for printing the cold plates. The printing process and the green part state of a cold plate can be seen in Figure 4.6. The cold plates are made of copper material because of high thermal conductivity.

Four different copper cold plates (CP1, CP2, CP3 and CP4) are manufactured with four different cross sections (CS1, CS2, CS3, and CS4). Since the outer view of the

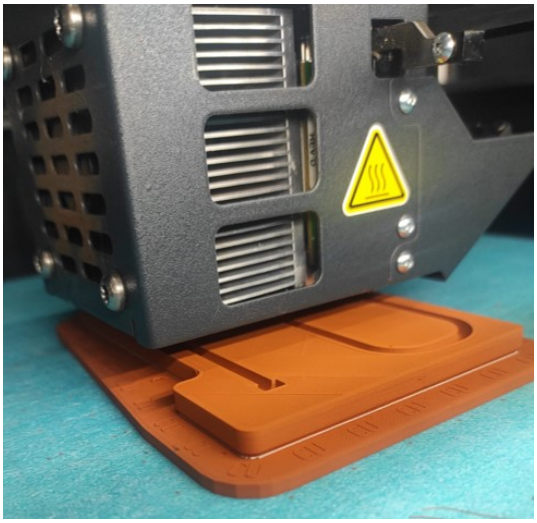

(a) Printing process of a cold plate on the Metal X 3D printer.

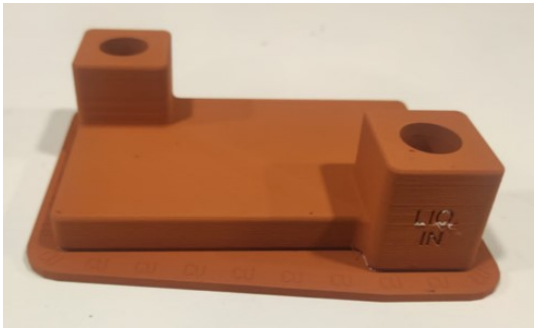

(b) Green part state of the printed cold plate.

Figure 4.6: The printing process and the green part state of the cold plate.

cold plates is the same, only one of the cold plates, CP1, is shown in Figure 4.7. The final masses of the cold plates and the mass values obtained in the CAD software are stated in Table 4.2. 0.9% to 2.5% differences are observed in terms of percentage, which are quite appropriate results for M-FFF when both binder and plastic removal is considered.

Figure 4.7: Fabricated cold plate.

Next, the final part is machined to assemble the quick couplings. First, two holes with

Table 4.2: Mass comparison of copper cold plates.

Cold Plate	Mass in CAD [g]	Actual Mass [g]	Difference
CP1	936.6	960.4	+2.5%
CP2	924.9	933.5	+0.9%
CP3	936.7	944.8	+0.9%
CP4	935.0	946.8	+1.3%

a diameter of 14 mm on the cold plate are drilled to 15 mm diameter (Figure 4.8a) which is a convenient material removal indicated as 0.2 to 0.5 mm with vertical machining in the design guide of Metal X 3D printer [42]. Then the threading operation is performed on the liquid inlet and outlet holes (Figure 4.8b). After the threading operation, male and female couplings are assembled on the G3/8 threaded holes of the cold plate. Assembly of the quick couplings and the cold plate can be seen in Figure 4.8c.

(a) Holes are enlarged with a tap drilling operation.

(b) Threading on the liquid entrance and exit holes.

(c) Assembly of the quick couplings and the cold plate.

Figure 4.8: Machining operations and the assembly of cold plates.

4.2 Testing of the Cold Plates

Proposed cold plate designs (CP1, CP2, CP3, and CP4) are subjected to experimental analyses to evaluate their thermal properties. A cold plate, named FSW is fabricated with the FSW method to serve as an example of traditional manufacturing methods (Figure 4.9).

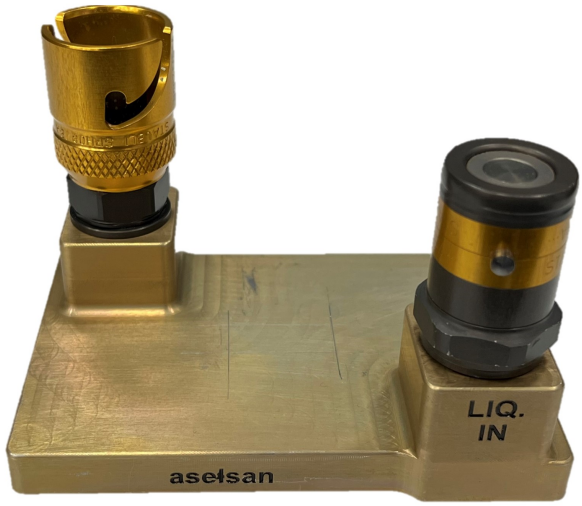

Figure 4.9: Example cold plate manufactured via FSW method.

First, the pressure drop values of the cold plate channels are measured experimentally with a device that supplies a continuous flow throughout the cold plates. Later on, temperature mapping and the maximum temperature observed on the resistor assembled on the cold plates are monitored using thermocouples and a thermal camera. Differences in temperatures according to the cold plates with different channel cross-sections are evaluated. Main aim of the tests is to evaluate the cold plates manufactured with M-FFF. Results of the FSW case is obtained to give an insight into the cold plates that are manufactured with traditional methods. The design of FSW is also different from other cold plates manufactured with M-FFF in terms of cold plate thickness and outer dimensions due to the limits of the FSW tool and the liquid channel since only a rectangular cross-section can be manufactured. However, the cross-section perimeter is adjusted as 20 mm (8 mm width and 2 mm height), which is close to the average cross-section perimeter of the cold plates manufactured via the

M-FFF method.

4.2.1 Experimental Analyses for Pressure Drop

Pressure drop values are evaluated to determine the capacity and largeness of the pump that supplies the fluid into the cold plates or manifolds connected in serial or parallel in the system. The largeness of the pump limits the design and positioning of the Flow Control Unit (FCU). Thus, initial pressure drop tests are essential to calculate the pressure drop and determine the pump properties.

For experimental analyses of the cold plates, an FCU is used. The cold plates are connected to the unit with proper hoses. Hoses have Wika O-10 pressure sensors before the liquid inlet section and after the liquid exit section of the cold plate, therefore pressure values are transmitted to the unit to see pressure drop values for the cold plates. The pressure drop experiment setup can be seen in Figure 4.10.

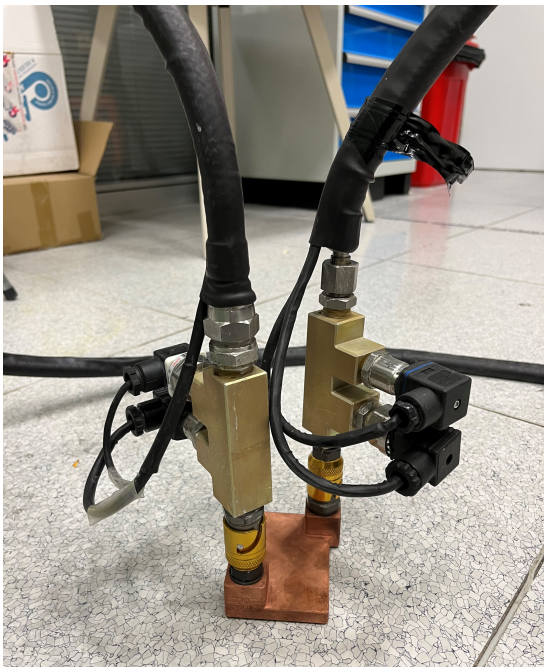

Figure 4.10: Experimental test setup of the cold plates for pressure drop.

Experiments are conducted with an FCU for four cold plate designs. For liquid, a mixture that includes monoethylene glycol and distilled water is used. Antifrogen N product of Clariant, which is compatible with copper materials, is used for mo-

noethylene glycol in the mixture, and it includes corrosion inhibitors to provide effective protection against corrosion. Experiment results are tabulated in Table 4.3. Experimental pressure drop results of cold plates are demonstrated in Figure 4.11 to show the difference between them. CP2, which has a triangular cross-section, has the minimum pressure drop values than the other manufactured cold plates according to the results.

Table 4.3: Pressure drop results according to the experiments.

	Pressure Drop [bar]				
Flow Rate [lpm]	**CP1**	**CP2**	**CP3**	**CP4**	**FSW**
2	0.6	0.4	0.9	0.9	0.5
3	1.1	0.7	1.6	1.5	0.9
4	1.7	1.1	2.6	2.4	1.3
5	2.5	1.6	3.5	3.6	1.8
6	3.3	2.1	4.8	5.0	2.5

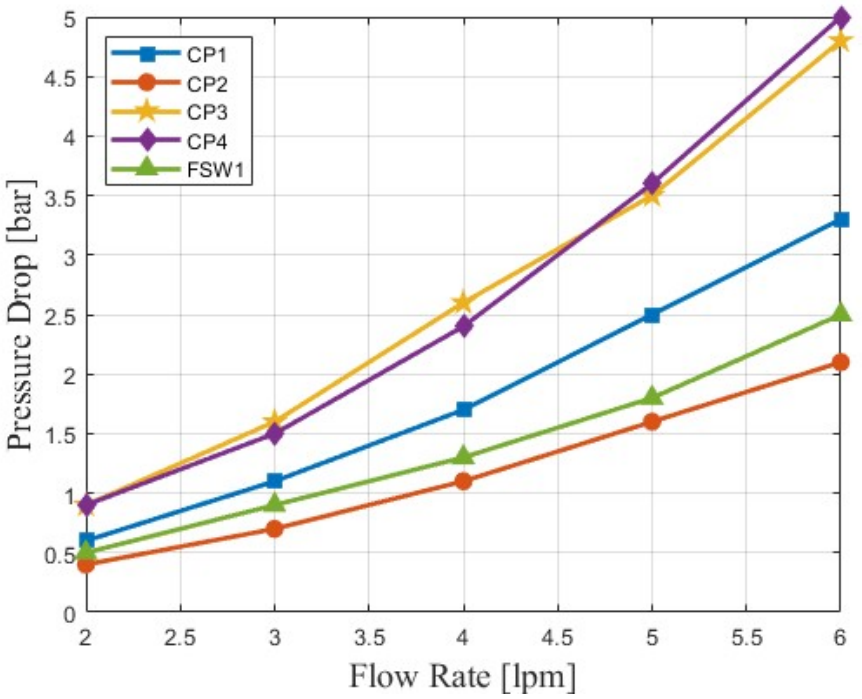

Figure 4.11: Comparison of pressure drop values of the manufactured cold plates.

4.2.2 Temperature Mapping

One of the control methods to investigate a cold plate's thermal performance is the functional tests. Since a cold plate helps to cool down the electronic cards or units due to the interior liquid channels, necessary units can be assembled on it and temperature limit and distribution can be checked. Since all the components on the electronic cards have operational temperature limits, electro-mechanical assemblies must be controlled in terms of temperature during prototyping.

In this part, proposed copper cold plate designs are tested for the maximum temperature observed and temperature distribution to check their ability about cooling. The cold plates are connected to the FCU with hoses to supply the required flow rate for cooling. A resistance, which simulates the heat dissipation of an electronic card, is assembled on the cold plate to check the maximum temperature observed on it. Also, the temperature distribution on the cold plate is checked using a thermal camera.

A test setup is constituted for temperature mapping tests of four cold plate designs. The cold plate that will be tested is connected to the FCU with appropriate hoses. A resistor, which is assembled on the cold plate, is used as a heat source. The resistance of 10Ω and an operating temperature range of -55°C to +150°C is chosen for the resistor of Florida RF Labs. The voltage to actuate the resistor is adjusted using a DC power supply with a 50V/4A limit. Before starting the tests, the temperature of the resistor is measured in the free state with a given voltage. Initially, 5V is given to the resistor and the temperature is raised constantly. Voltage output is closed down when the temperature on the resistor is read close to 150°C which is the maximum operating temperature for the resistor. When 20V is applied on the resistor, faster temperature raise is observed. As it is seen, the maximum temperature observed on the resistor is not limited by the given voltage values, it is limited by the maximum operating temperature of the resistor.

The resistor is assembled on the top face of the cold plate. A 0.5 mm thermal pad with high conductivity is located between the resistor and the top face of the cold plate to eliminate the gaps between two faces that can occur due to surface roughness and low flatness. Before testing, an apparatus is used to pull down and improve contact of the

resistor with the cold plate. Since both sides of the thermal pad are sticky, high contact of the resistor is provided after removing the apparatus during testing. Three T-type thermocouples of Omega are taped on the top face of the resistor, where the maximum temperature is expected. Temperature values obtained with the thermocouples are read using an Omega OM-HL-EH-TC Data Logger. The cold plate is placed inside a 3D printed plastic part that covers all outer faces of the cold plate with 4 mm thickness for insulation except the top face of it which is a common use case of cold plates in radar systems. Temperature mapping on the faces of the cold plate and the resistor is monitored with an Optris PI400 Infrared Camera. The top face of the cold plate is kept open when placed on a plastic insulation part to monitor temperature distribution with the thermal camera. Therefore, thermocouple measurement is performed with the same condition to compare results in a better way. The test setup for the temperature mapping can be seen in Figure 4.12.

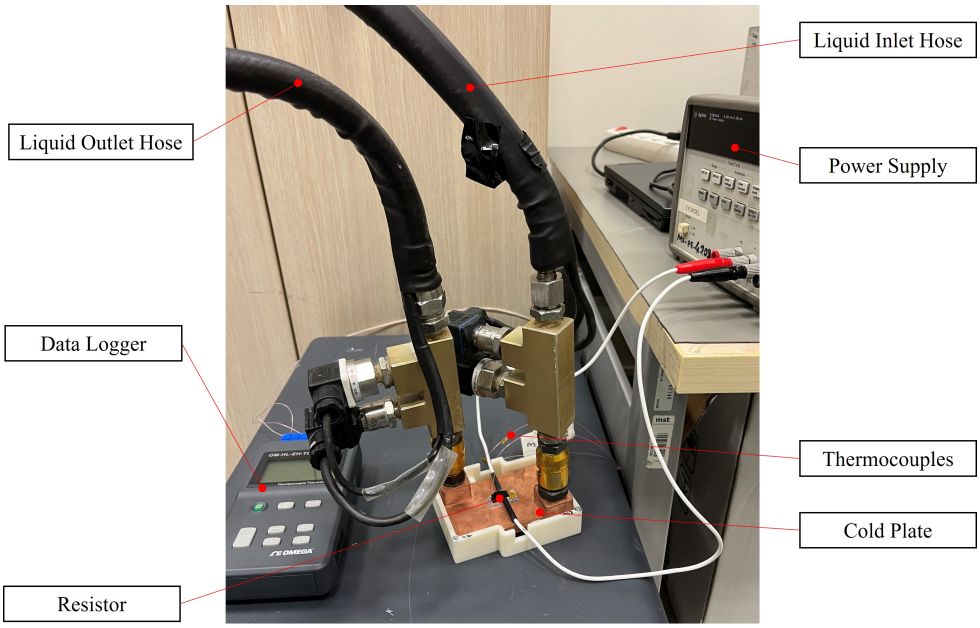

Figure 4.12: Experimental test setup of the cold plates for temperature mapping.

During the testing of the cold plates, 3 lpm is chosen for the flow rate since it is an appropriate value for the tests of commonly used cold plates. Ambient temperature is measured as $25 \pm 1.1°C$ throughout the tests. Liquid inlet temperature is set to 25°C in the FCU which has the uncertainty value of $\pm 0.3°C$. Before supplying voltage from the power supply to the resistor, the liquid is provided to the cold plate to reach a

stable flow. Four different voltage values are given to the resistor to observe temperature mapping and the maximum temperature with changing power of the resistor. 5V, 10V, 15V, and 20V are tried to be supplied to the resistor corresponding to 2.5W, 10W, 22.5W, and 40W, respectively. In CP3 and CP4, monitored temperatures are close to the operational limit of the resistor at 32.4W (18V), therefore 40W (20V) is not supplied. Also, 40W (20V) is not supplied to CP2 because of the same condition. Therefore, 36.1W (19V) is supplied. Higher voltage values are not used since the operating temperature range of the resistor could be exceeded. According to these parameters, temperature values on the top face of the resistor are obtained with thermocouple measurement, and temperature mapping on the cold plate is observed with the thermal camera. Temperature values are noted when no temperature change is monitored on the thermocouple data logger. During testing, constant temperatures on the top face of the resistor are observed, which means cold plates are able to keep the resistor at a constant temperature.

4.2.2.1 CP1

For the CP1, temperature mapping on the cold plate for four different power values is monitored via thermal camera and results can be seen in Figure 4.13. According to this monitoring, the maximum temperatures are observed for 2.5W, 10W, 22.5W, and 40W cases at 3 lpm. During monitoring, thermocouple data is noted simultaneously. The maximum observed temperature on the top face of the resistor is read from the data logger and monitored with the thermal camera; the temperature of the liquid outlet viewed from the FCU is indicated in Table 4.4. Also, the average temperature on a specific area of the cold plate is monitored with a thermal camera, and the results are tabulated on Table 4.4.

4.2.2.2 CP2

For the CP2, temperature mapping on the cold plate for four different power values is monitored via thermal camera and results can be seen in Figure 4.14. According to this monitoring, the maximum temperatures are observed for 2.5W, 10W, 22.5W, and

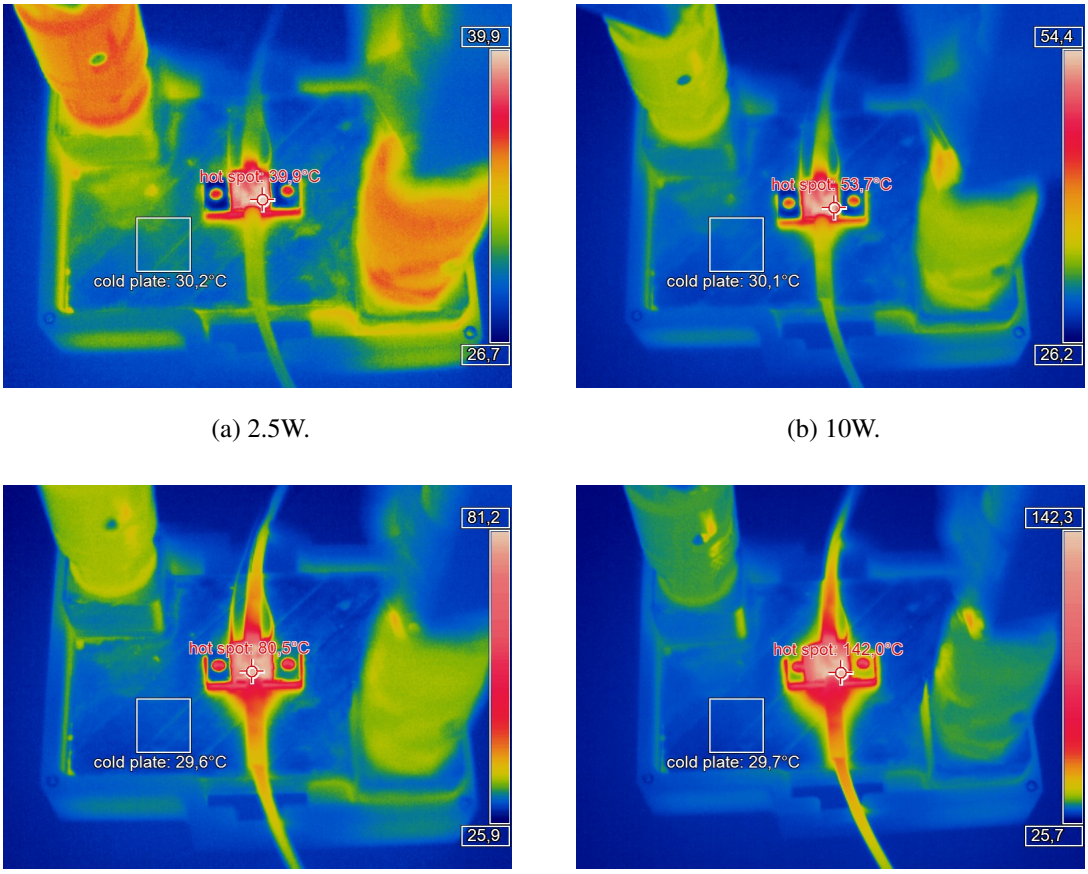

(a) 2.5W.

(b) 10W.

(c) 22.5W.

(d) 40W.

Figure 4.13: Temperature mapping on CP1 for different power inputs.

Table 4.4: The maximum temperatures viewed on the resistor and the liquid outlet for CP1.

Power [W]	**Thermocouple readings [°C]**	**Thermal camera readings [°C]**	**Specific area on cold plate [°C]**	**Liquid outlet [°C]**
2.5	39.0	39.9	30.2	33.5
10	52.7	53.7	30.1	33.7
22.5	79.1	80.5	29.6	34.0
40	140.8	142.0	29.7	34.4

36.1W cases at 3 lpm. During monitoring, thermocouple data are noted simultaneously. The maximum observed temperature on the top face of the resistor is read from the data logger and monitored with the thermal camera; the temperature of the liquid outlet viewed from the FCU is indicated in Table 4.5. Also, the average temperature on a specific area of the cold plate is monitored with a thermal camera and tabulated.

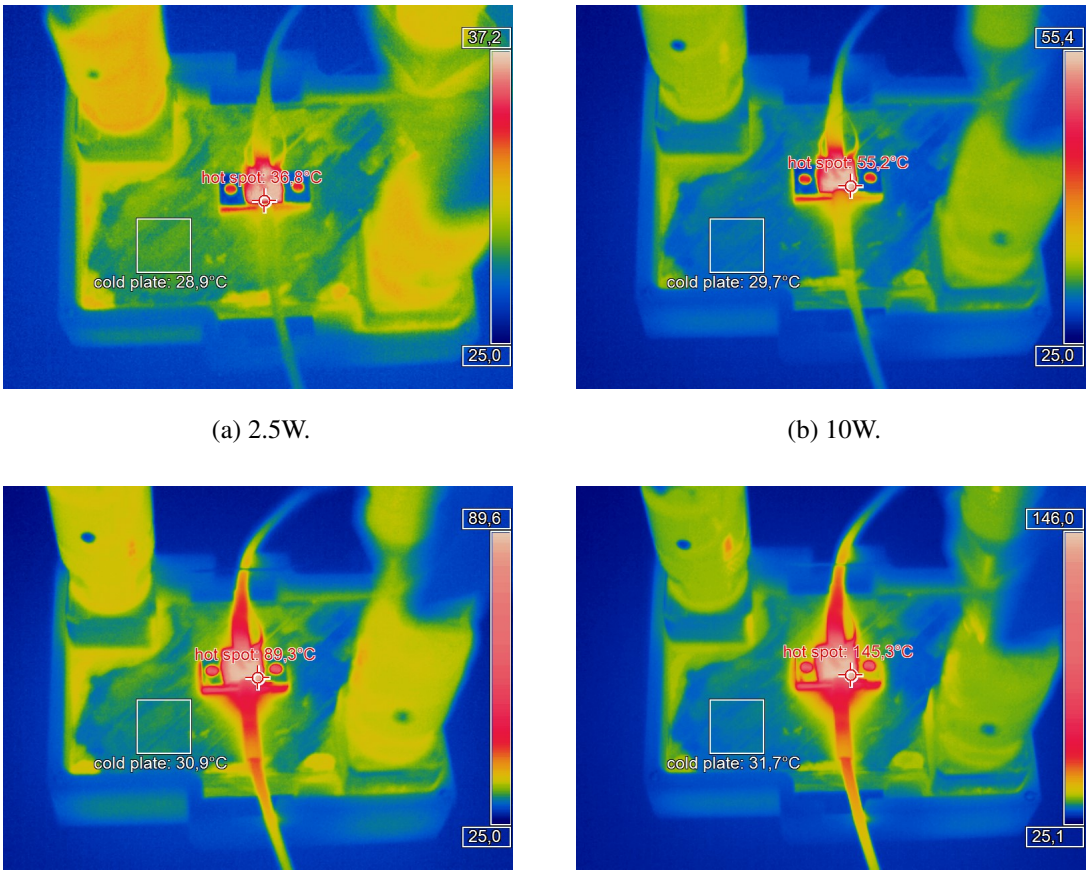

(a) 2.5W.

(b) 10W.

(c) 22.5W.

(d) 36.1W.

Figure 4.14: Temperature mapping on CP2 for different power inputs.

4.2.2.3 CP3

For the CP3, temperature mapping on the cold plate for four different power values is monitored via thermal camera and results can be seen in Figure 4.15. According to this monitoring, maximum temperatures are observed for 2.5W, 10W, 22.5W, and 32.4W cases at 3 lpm. During monitoring, thermocouple data are noted simultane-

Table 4.5: The maximum temperatures viewed on the resistor and liquid outlet for CP2.

Power [W]	**Thermocouple readings [°C]**	**Thermal camera readings [°C]**	**Specific area on cold plate [°C]**	**Liquid outlet [°C]**
2.5	36.2	36.8	28.9	33.4
10	55.1	55.2	29.7	33.8
22.5	88.8	89.3	30.9	34.3
36.1	141.4	145.3	31.7	34.7

ously. The maximum observed temperature on the top face of the resistor is read from the data logger and monitored with the thermal camera; the temperature of the liquid outlet viewed from the FCU is indicated in Table 4.6. Also, the average temperature on a specific area of the cold plate is monitored with a thermal camera and tabulated.

Table 4.6: The maximum temperatures viewed on the resistor and liquid outlet for CP3.

Power [W]	**Thermocouple readings [°C]**	**Thermal camera readings [°C]**	**Specific area on cold plate [°C]**	**Liquid outlet [°C]**
2.5	39.0	39.4	28.9	33.3
10	60.3	62.5	29.6	33.4
22.5	99.9	103.1	30.1	34.4
32.4	144.2	147.9	30.7	35.9

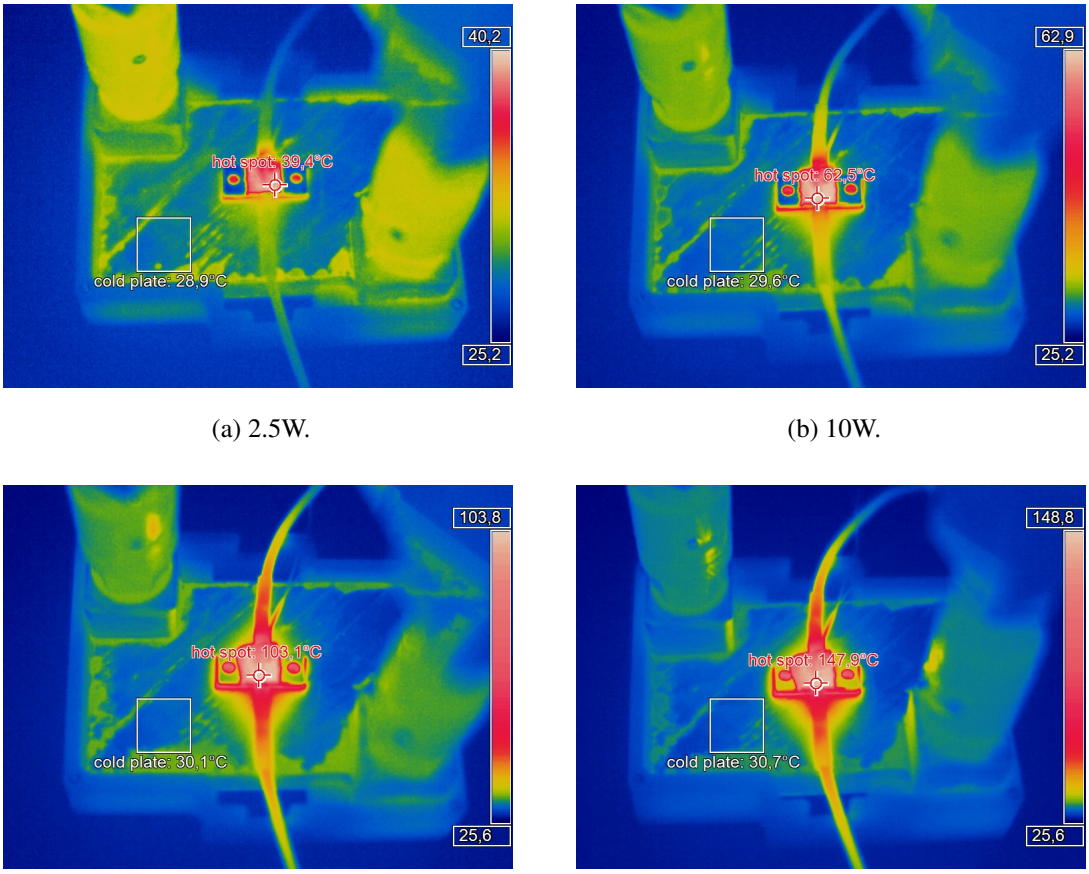

(a) 2.5W.

(b) 10W.

(c) 22.5W.

(d) 32.4W.

Figure 4.15: Temperature mapping on CP3 for different power inputs.

4.2.2.4 CP4

For the CP4, temperature mapping on the cold plate for four different power values is monitored via thermal camera and results can be seen in Figure 4.16. According to this monitoring, maximum temperatures are observed for 2.5W, 10W, 22.5W, and 32.4W cases at 3 lpm. During monitoring, thermocouple data are noted simultaneously. The maximum observed temperature on the top face of the resistor is read from the data logger and monitored with the thermal camera; the temperature of the liquid outlet viewed from the FCU is indicated in Table 4.7. Also, the average temperature on a specific area of the cold plate is monitored with a thermal camera and tabulated.

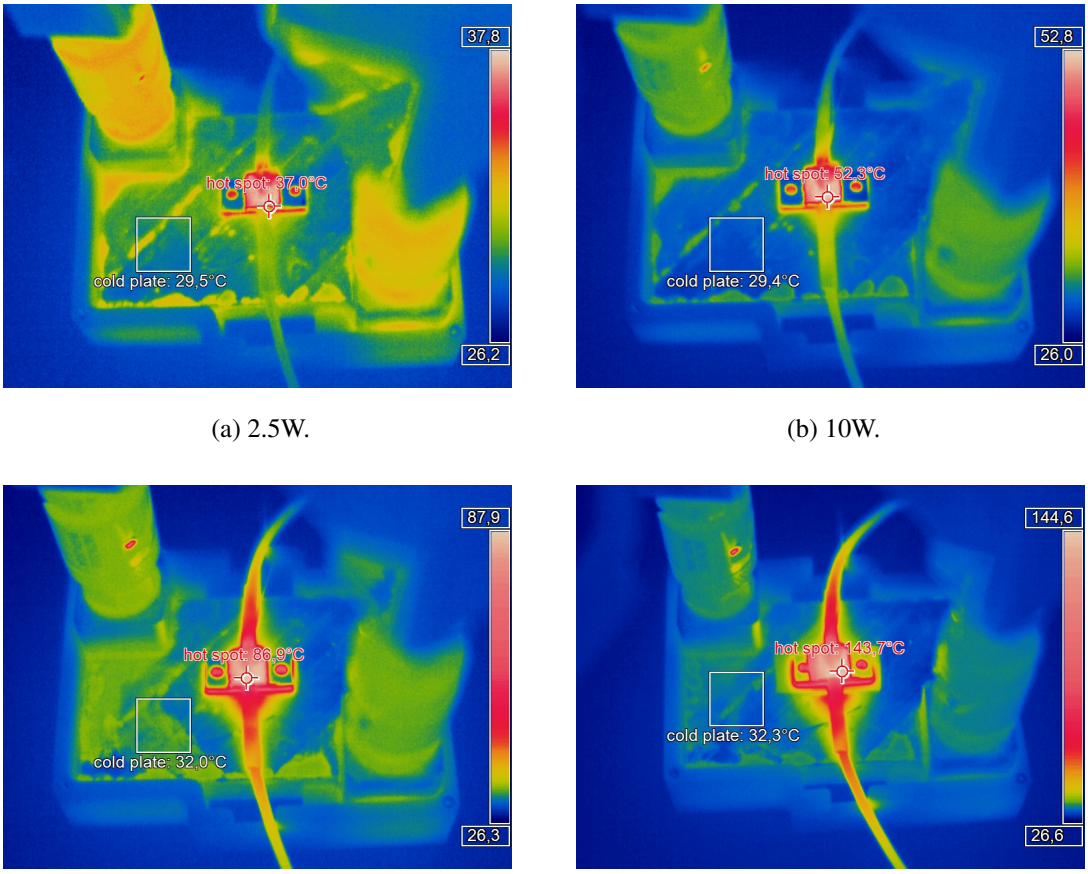

(a) 2.5W.

(b) 10W.

(c) 22.5W.

(d) 32.4W.

Figure 4.16: Temperature mapping on CP4 for different power inputs.

Table 4.7: The maximum temperatures viewed on the resistor and liquid outlet for CP4.

Power [W]	**Thermocouple readings [°C]**	**Thermal camera readings [°C]**	**Specific area on cold plate [°C]**	**Liquid outlet [°C]**
2.5	36.1	37.0	29.5	33.0
10	50.1	52.3	29.4	34.2
22.5	83.4	86.9	32.0	34.9
32.4	141.6	143.7	32.3	36.0

4.2.2.5 FSW

For the FSW, temperature mapping on the cold plate for four different power values is monitored via thermal camera and the results can be seen in Figure 4.17. According to this monitoring, the maximum temperatures are observed for 2.5W, 10W, 22.5W, and 40W cases at 3 lpm. During monitoring, thermocouple data are noted simultaneously. The maximum observed temperature on the top face of the resistor is read from the data logger and monitored with the thermal camera; the temperature of the liquid outlet viewed from the FCU is indicated in Table 4.8. Also, the average temperature on a specific area of the cold plate is monitored with a thermal camera and tabulated.

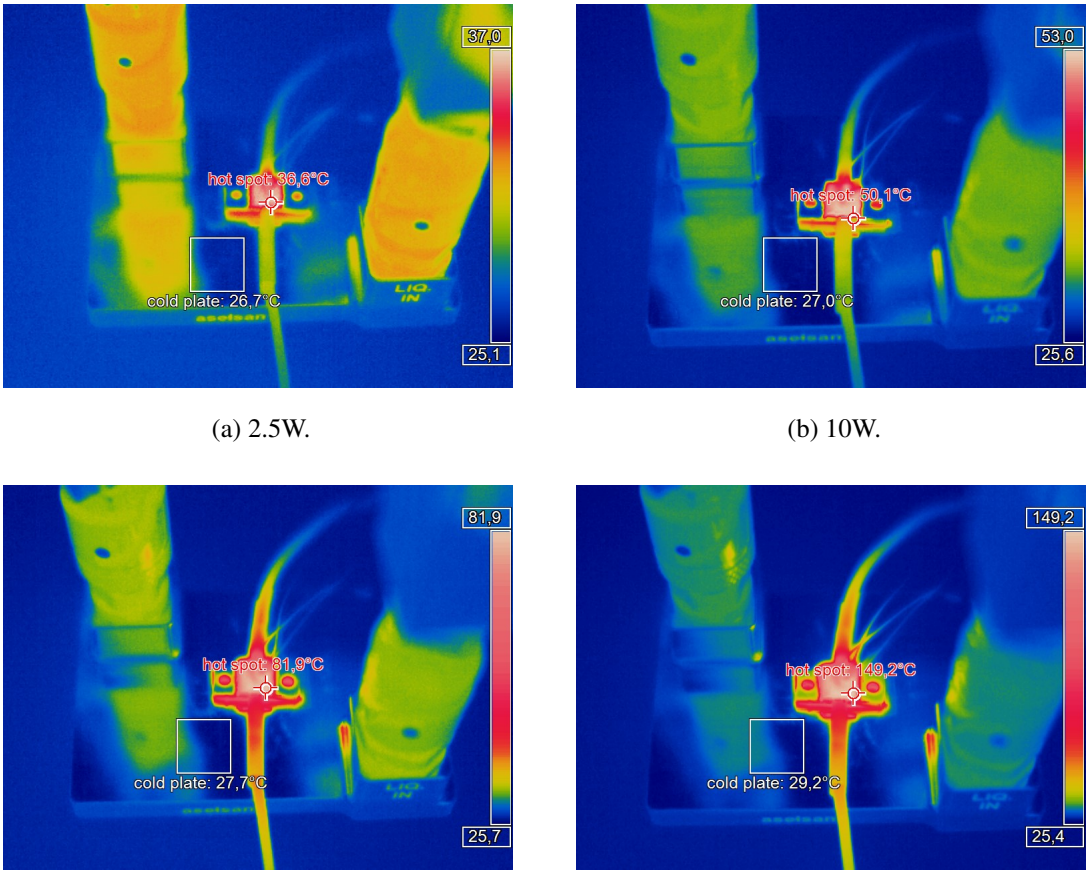

(a) 2.5W.

(b) 10W.

(c) 22.5W.

(d) 40W.

Figure 4.17: Temperature mapping on the FSW case for different power inputs.

Table 4.8: The maximum temperatures viewed on the resistor and the liquid outlet for FSW.

Power [W]	**Thermocouple readings [°C]**	**Thermal camera readings [°C]**	**Specific area on cold plate [°C]**	**Liquid outlet [°C]**
2.5	36.5	36.6	26.7	33.0
10	51.5	50.1	27.0	33.2
22.5	81.5	81.9	27.7	33.6
40	146.4	149.2	29.2	33.8

4.2.2.6 Results and Comparison

For the stated results in this part, the maximum temperature on the resistor is acquired from the thermocouples. Results of specific areas on the cold plates are obtained from the thermal camera monitoring. In addition to this, the maximum temperature on the resistor is checked using the thermal camera to compare the results with thermocouple readings. Sensitivity, focus, accuracy, and distance settings of the thermal camera, and contact or placement problems of the thermocouples could be the reasons for monitored temperature differences in both types of equipment. According to the obtained results, the maximum observed temperatures on the resistor at 3 lpm are compared in Figure 4.18 with changing heat loads. The temperature of the liquid outlet increases with increasing power inputs. But no correlation between the temperature of the liquid outlet and the cold plate design is noticed which occurs due to the cooling performance of the FCU itself and the operation parameters of the fan located in the FCU.

During testing with specific power input, all test conditions are kept the same except for the cold plane designs. According to the observed temperatures on the resistor, CP1, which has a cross-section as a droplet shape, has a lower maximum temperature than other cold plates with increasing power inputs. For the 2.5W power input, the maximum temperatures are observed close. Since increasing power inputs make it

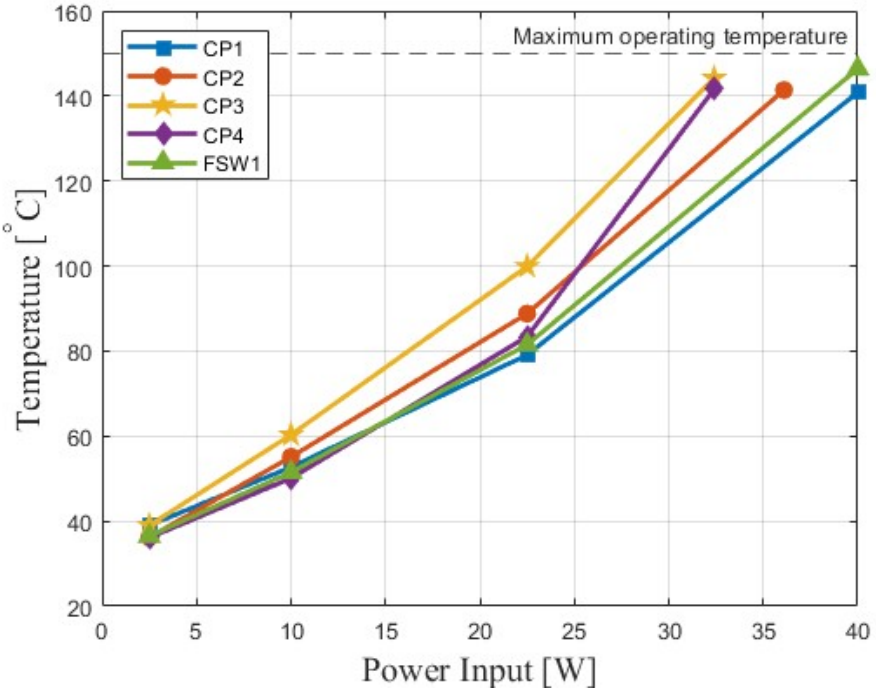

Figure 4.18: Comparison of the maximum observed temperatures on the resistor at 3 lpm. Dashed line indicates the maximum operating temperature of the resistor.

easier to differentiate the thermal performance of the cold plates, observed maximum temperatures are started to distinct after a power input of 10W. Higher temperatures are observed at CP2, CP3, and CP4 in high power input values, therefore tests ended at 36.1W (CP2) and 32.4W (CP3 and CP4) not to exceed the maximum operating temperature of the resistor. A direct correlation according to the section area of the cross-sections is not detected. Lower temperature readings are monitored as the section perimeter of the channel cross-section decreases. This result is based upon different flow characteristics originating due to the different cold plate designs. More developed flow or flow with fewer dead zones in CP1 than the other cold plates could be the reason for better outcomes. Regarding the FSW cold plate, the results obtained are highly similar to the CP1 design. Although aluminum is the material of the FSW, its low thickness compared to the M-FFF ones improved its performance. Since the perimeter of the channel cross-section of the FSW cold plate is more than the perimeters of the CP1 and the CP2 cases, the heat transfer capability of the FSW is higher. According to these results, the CP1 design can be considered as the best design for

the liquid cooling of electronic components where cold plates are manufactured with M-FFF and supportless manufacturing is considered.

4.2.3 Uncertainty Analysis

An experimental approach is considered during the thermal performance tests of the cold plates. Uncertainties of the parameters in the experiments are obtained or calculated. Experimental uncertainty is found according to the single data measurements both for the pressure drop and the temperature measurements. Uncertainties of the results obtained for the pressure drop and the temperature mapping are limited by the accuracy of the measuring instruments.

Pressure drop (ΔP) values are measured by taking the difference of two pressure values which is stated in Equation 4.1. Pressure sensor's uncertainty is found as $\pm$0.05 bar from the datasheet [45]. Since there is a subtraction between two sensor outputs, total uncertainty in the pressure drop is found as $\pm$0.1 bar.

$$\Delta P = P_{inlet} - P_{outlet} \tag{4.1}$$

Since T-type thermocouples are used during measurement of temperatures on the resistor, uncertainty is obtained as $\pm$0.5°C from the datasheet [46]. Thermal camera used to monitor the temperature distribution on the cold plates has an uncertainty value of $\pm$2°C which is obtained from [47].

For the flow rate, the uncertainty of $\pm$0.1 lpm is determined according to the turbine type of flowmeter that is used to read the flow rate. Uncertainties of the ambient temperature and the liquid inlet temperature are determined as $\pm$1.1°C and $\pm$0.3°C, respectively. These determined uncertainties for different test parameters and results are stated in Table 4.9.

The power input that is applied to the resistor, is read from the power supply according to the voltage and current values with the following equation

Table 4.9: Determined uncertainties for different test parameters.

Test parameter	Unit	Measurement	Uncertainty
Pressure drop	bar	Pressure sensor	±0.1
Temperature on the resistor	°C	T-type Thermocouple	±0.5
Temperature on the cold plate	°C	Thermal camera	±2
Flow rate	lpm	Flowmeter	±0.1
Ambient temperature	°C	J-type Thermocouple	±1.1
Liquid inlet temperature	°C	Temperature sensor	±0.3

$$P = IV \tag{4.2}$$

where P is power input, I is current and V is voltage. According to observations, uncertainties of current and voltage are determined as ±0.01 A and ±0.15 V, respectively. Uncertainty of the power input is calculated according to the following general equation.

$$F = \sqrt{\left(\frac{\delta F}{\delta X1}Y1\right)^2 + \left(\frac{\delta F}{\delta X2}Y2\right)^2 + ...\left(\frac{\delta F}{\delta Xn}Yn\right)^2} \tag{4.3}$$

Uncertainty results for different power inputs used in the temperature mapping tests are calculated according to Equation 4.2 and Equation 4.3; and tabulated in Table 4.10. Uncertainty accumulation can be seen from the uncertainty results of power inputs in the table.

4.2.4 Performance Ratings of the Cold Plates

After the results are obtained from the pressure drop and the temperature measurements, a comparison matrix is constituted for the cold plates. Attributes related to the thermal performance are used for rating. These attributes are determined as pressure drop, temperature on the resistor, temperature of the liquid inlet, and temperature on

Table 4.10: Calculated uncertainties for different power inputs.

Current [A]	**Voltage [V]**	**Power input [W]**
0.5 ± 0.01	5 ± 0.15	2.5 ± 0.09
1.0 ± 0.01	10 ± 0.15	10 ± 0.18
1.5 ± 0.01	15 ± 0.15	22.5 ± 0.27
1.8 ± 0.01	18 ± 0.15	32.4 ± 0.33
1.9 ± 0.01	19 ± 0.15	36.1 ± 0.34
2.0 ± 0.01	20 ± 0.15	40.0 ± 0.36

a specific point of the cold plate. The relative importance of 0.5 is assigned for the temperature on the resistor since temperature limits are the most important factor to be monitored. The second important attribute is selected as the pressure drop with 0.3 of relative importance, which directly affects the largeness of the pump in the system. The third attribute is chosen as the temperature on a specific point of the cold plate with 0.15 of relative importance since temperature around the cold plate can affect the suitability of the assembled parts. The temperature of the liquid outlet is picked as the least important merit with 0.05 of relative importance since the outlet temperatures are close to each other and the FCU system can tolerate these observed values. Since the results of these attributes are desired to be minimum, low preference is assigned for all. According to these, rating criteria are stated in Table 4.11.

Table 4.11: Rating criteria with respect to the attributes.

Property	**Units**	**Rel. Imp.**	**Low**	**High**	**Pref.**
Pressure drop	bar	0.3	0.5	1.8	Low
Temp. on the resistor	°C	0.5	75	105	Low
Temp. of the liquid outlet	°C	0.05	33	35.5	Low
Temp. on the cold plate	°C	0.15	25	35	Low

Results according to these rating criteria are shown in Table 4.12. For temperature

values, results obtained for the 22.5W power input are used. Values of 3 lpm condition are used both for the pressure drop tests and the temperature measurements. According to the rating results, FSW has the best rating of all the manufactured cold plates. Since it has lower cold plate thickness and longer channel section perimeter than the cold plates manufactured with the M-FFF method, thermal performance is affected positively although it is made of aluminum material compared to copper material that is used in the cold plates fabricated with M-FFF.

In this work, the focus is on the thermal performance of the cold plates manufactured with the M-FFF method. Therefore, comparison of the proposed cold plate designs manufactured via M-FFF method is the main aim. According to the rating results, the CP1 case, which has the shape of a droplet cross-section, has the best rating among the other cold plates manufactured with the M-FFF method. It has an average value of pressure drop result and the best result for the temperature on the resistor. According to the relative importance coefficients, the best overall rating of 0.704 belongs to the CP1 case.

Table 4.12: Rating results of the cold plates.

Property	**CP1**	**CP2**	**CP3**	**CP4**	**FSW**
Pressure drop [bar]	1.1	0.7	1.6	1.5	0.9
Temp. on the resistor [°C]	79.1	88.8	99.9	83.4	81.5
Temp. of the liquid outlet [°C]	34.0	34.3	34.4	34.9	33.6
Temp. on the cold plate [°C]	29.6	30.9	30.1	32.0	27.7
Overall Rating	**0.704**	**0.609**	**0.227**	**0.486**	**0.747**

CHAPTER 5

DISCUSSIONS & CONCLUSION

In this thesis, copper cold plates are designed and fabricated via the M-FFF method, a novel AM technology. Conditions and limitations for design and fabrication are described. Thermal performance parameters for the cold plates such as pressure drop and temperature mapping are observed. Results are obtained with numerical and experimental analyses. To evaluate the performance of the M-FFF method, various characterization and quality tests are conducted. According to these results, advantageous and disadvantageous of the M-FFF process are detected.

Since M-FFF is a newly introduced method, there are many questions about the process to be discovered. It was challenging to fabricate a cold plate via the M-FFF method since it is a complex and problematic part due to its function and relation with liquid. As stated before, the point of origin of this approach is producing metal parts with cheaper platforms and using the design freedom of AM methods instead of the traditional methods. Besides, process costs are high in the traditional methods due to some specialized components such as machines, tools, furnaces, and chemicals. In addition to these, accessibility to these methods in Turkey is limited and creates a bottleneck in fabrication. All these stated reasons pushed and motivated us to find an alternative method.

Before production in M-FFF, the performance of the process is tried to be understood with various tests. The advantages of the process are discovered by conducting CMM, surface roughness measurements, and porosity analyses. According to these obtained results, necessary improvements are applied on the process before the cold plate fabrication.

Dimensional accuracies are obtained well enough in the M-FFF process, which is an important parameter when an assembly is considered for the final part. Quick couplings, PCBs, and other related mechanics can be assembled into final parts produced with M-FFF since dimensional tolerances and position correctness is not bad. According to surface roughness measurements, results are slightly worse than CNC quality, but when compared to other AM methods producing metal parts, such as SLM, results are much better. This means that AM methods can be used to produce metal cold plate parts since pressure drop will not be affected too much due to the acceptable Ra and Rz values. These results also affect the card assembly of the cold plate positively due to the high quality of contact areas. According to thermal conductivity measurement, the result is acceptable to use produced copper parts with M-FFF in thermal applications. Porosity results are obtained with Archimedes method, SEM analyses, and Micro-CT scans. It is found that relative density values according to the porosity analyses are close to datasheet results. According to the X-ray scans of the parts, any burrs or residuals of support structures are not seen which is a commonly encountered problem. The porosity of the part and distortions throughout the part are observed with Micro-CT analyses. It is seen that monitored porous zones are usually located on the start-stop points of the nozzle during covering a layer. Consequently, the nozzle path parameter must be paid attention to and improved when necessary before the fabrication of a part. When the coverage path is not well adjusted, porous zones can be encountered frequently which is a problem for the cold plates. Leakage and fracture problems can occur when pressurized liquid is used.

Cold plates are fabricated according to knowledge obtained in the performance evaluation tests conducted for the M-FFF process. Copper material is used because of its advantageous properties in thermal applications. Cold plate designs with four different channel cross-sections are fabricated with the M-FFF method and compared according to their thermal performances. A cold plate is also manufactured using FSW method with aluminum material to serve as an example. Pressure drop results are measured to see the particular effects of the cold plates on the largeness of the pump. The lowest pressure drop results are obtained for the CP2 design, which has a triangle cross-section.

By placing a heat source on the cold plates and passing the liquid through it, temper-

ature mapping is monitored with a thermal camera. The heat source is replicated as a heating component on a PCB and cooling performance regarding the channel cross-section is observed. The lowest temperatures around the heat source with increasing power inputs are observed in the CP1 case, which has the lowest cross-section perimeter compared to the other cold plate designs. These temperatures are measured with thermocouples attached to the heat source, and convenient results compared to the thermal camera monitoring are obtained. Temperatures on some areas of the cold plates are also monitored. The cold plate manufactured with FSW method has the second best temperature results with close values to the CP1 case. According to the observed temperature results, the best performance is obtained with the CP1 case which has a droplet cross-section and it is seen that the proposed cold plate designs can be used for cooling applications of electronics.

According to the pressure drop and temperature measurements, performance ratings of cold plates are calculated with different relative importance coefficients. The FSW design has the highest rating with 0.747 since both pressure drop and temperature on the resistor are low. Since FSW design is an example and main aim is comparing cold plates manufactured with M-FFF, comparison is done for the proposed cold plate designs. Therefore, the CP1 case, which has a droplet cross-section, has the best rating of 0.704 among the other cold plates manufactured with the M-FFF method.

By taking advantage of design freedom, the M-FFF process can be used for thermal applications and cold plate productions. Since there are some unknown parameters about the process, parts can be fabricated for fast-prototyping purposes. When traditional methods are limited and hard to reach for cold plate manufacturing, a cheaper and more accessible method of M-FFF can be an alternative approach to be used. Also, an insight is constructed for the M-FFF process, and integration of new materials that are introduced for the M-FFF method can be easier according to the outcomes obtained in this study.

For future works, the performance of the M-FFF process can be investigated in more detail in terms of structural and thermal properties. Coupled thermal analyses can be performed to measure pressure drop and temperatures to compare with the experimental results. Comparison between cold plates manufactured with M-FFF, SLM,

and traditional methods can be performed. Enhancement of the fill path in the CAM software step can affect reducing the porosity percent in the part. Mass reduction for the parts can be performed with changing infill structures. More organic and generic shapes can be integrated to channel geometries to increase both thermal properties and mass reduction.

REFERENCES

[1] Markforged, "Learning library - 3d printing process," 2022. https://markforged.com/resources/learn/3d-printing-basics, Last accessed on 2023-01-15.

[2] B. Redwood, F. Schöffer, and B. Garret, *The 3D printing handbook: technologies, design and applications*. 3D Hubs, 2017.

[3] D. Bacellar, V. Aute, Z. Huang, and R. Radermacher, "Design optimization and validation of high-performance heat exchangers using approximation assisted optimization and additive manufacturing," *Science and Technology for the Built Environment*, vol. 23, no. 6, pp. 896–911, 2017.

[4] A. B. Spierings, M. u. Schneider, and R. Eggenberger, "Comparison of density measurement techniques for additive manufactured metallic parts," *Rapid Prototyping Journal*, 2011.

[5] P. Minetola, L. Iuliano, and G. Marchiandi, "Benchmarking of fdm machines through part quality using it grades," *Procedia Cirp*, vol. 41, pp. 1027–1032, 2016.

[6] W. E. Frazier, "Metal additive manufacturing: a review," *Journal of Materials Engineering and performance*, vol. 23, no. 6, pp. 1917–1928, 2014.

[7] W. J. Sames, F. A. List, S. Pannala, R. R. Dehoff, and S. S. Babu, "The metallurgy and processing science of metal additive manufacturing," *International Materials Reviews*, vol. 61, no. 5, pp. 315–360, 2016.

[8] S. M. Thompson, Z. S. Aspin, N. Shamsaei, A. Elwany, and L. Bian, "Additive manufacturing of heat exchangers: A case study on a multi-layered ti–6al–4v oscillating heat pipe," *Additive Manufacturing*, vol. 8, pp. 163–174, 2015.

[9] J. Armen and H. A. Bruck, "Improving contact resistance in metal–ceramic heat exchangers running liquid metal by additive manufacturing and ceramic tubes

with electroplated films," *The International Journal of Advanced Manufacturing Technology*, vol. 113, no. 7, pp. 2101–2119, 2021.

[10] R. da Silva, M. Mortean, K. de Paiva, L. Beckedorff, J. Oliveira, F. Brandão, A. Monteiro, C. Carvalho, H. Oliveira, D. Borges, and V. Chastinet, "Thermal and hydrodynamic analysis of a compact heat exchanger produced by additive manufacturing," *Applied Thermal Engineering*, vol. 193, p. 116973, 2021.

[11] Z. Gobetz, A. Rowen, C. Dickman, K. Meinert, and R. Martukanitz, "Utilization of additive manufacturing for aerospace heat exchangers," tech. rep., Pennsylvania State University State College United States, 2016.

[12] J. Fernandes, S. Ghalambor, D. Agonafer, V. Kamath, and R. Schmidt, "Multi-design variable optimization for a fixed pumping power of a water-cooled cold plate for high power electronics applications," in *13th InterSociety Conference on Thermal and Thermomechanical Phenomena in Electronic Systems*, pp. 684–692, IEEE, 2012.

[13] M. Pietropaoli, R. Ahlfeld, F. Montomoli, A. Ciani, and M. D'Ercole, "Design for additive manufacturing: Internal channel optimization," *Journal of Engineering for Gas Turbines and Power*, vol. 139, no. 10, 2017.

[14] P.-H. Tseng, K.-T. Tsai, A.-L. Chen, and C.-C. Wang, "Performance of novel liquid-cooled porous heat sink via 3-d laser additive manufacturing," *International Journal of Heat and Mass Transfer*, vol. 137, pp. 558–564, 2019.

[15] A. C. Öncel and U. Yaman, "Generation of optimized voronoi based interior structures for improved mechanical properties," *Procedia Manufacturing*, vol. 38, pp. 42–51, 2019.

[16] T. C. Henry, M. A. Morales, D. P. Cole, C. M. Shumeyko, and J. C. Riddick, "Mechanical behavior of 17-4 ph stainless steel processed by atomic diffusion additive manufacturing," *The International Journal of Advanced Manufacturing Technology*, vol. 114, no. 7, pp. 2103–2114, 2021.

[17] J. Rodriguez, J. Vicente, J. Ezeiza, A. Zuriarrain, P. Arrazola, X. Badiola, E. Dominguez, and D. Soler, "Mechanical and electrical properties of additively

manufactured copper," in *IOP Conference Series: Materials Science and Engineering*, vol. 1193, p. 012034, IOP Publishing, 2021.

[18] M. Galati and P. Minetola, "Analysis of density, roughness, and accuracy of the atomic diffusion additive manufacturing (adam) process for metal parts," *Materials*, vol. 12, no. 24, p. 4122, 2019.

[19] S. G. Kandlikar and C. N. H. II, "Liquid cooled cold plates for industrial high-power electronic devices—thermal design and manufacturing considerations," *Heat Transfer Engineering*, vol. 30, no. 12, pp. 918–930, 2009.

[20] Y. Zhang, X. Yu, Q. Feng, and R. Zhang, "Thermal performance study of integrated cold plate with power module," *Applied Thermal Engineering*, vol. 29, no. 17-18, pp. 3568–3573, 2009.

[21] S. Qian, W. Wang, C. Ge, S. Lou, E. Miao, and B. Tang, "Topology optimization of fluid flow channel in cold plate for active phased array antenna," *Structural and Multidisciplinary Optimization*, vol. 57, no. 6, pp. 2223–2232, 2018.

[22] C. Pfeiffer, J. Massman, and T. Steffen, "3-d printed metallic dual-polarized vivaldi arrays on square and triangular lattices," *IEEE Transactions on Antennas and Propagation*, vol. 69, no. 12, pp. 8325–8334, 2021.

[23] M. Cardone and B. Gargiulo, "Design and experimental testing of a mini channel heat exchanger made in additive manufacturing," *Energy Procedia*, vol. 148, pp. 932–939, 2018.

[24] R. Tiwari, R. S. Andhare, A. Shooshtari, and M. Ohadi, "Development of an additive manufacturing-enabled compact manifold microchannel heat exchanger," *Applied Thermal Engineering*, vol. 147, pp. 781–788, 2019.

[25] A. S. Sabau, A. Bejan, D. Brownell, K. Gluesenkamp, B. Murphy, F. List III, K. Carver, C. R. Schaich, and J. W. Klett, "Design, additive manufacturing, and performance of heat exchanger with a novel flow-path architecture," *Applied Thermal Engineering*, vol. 180, p. 115775, 2020.

[26] J. Boxleitner, T. Mulholland, and G. Nellis, "Air-to-liquid heat exchanger fabricated using deposition-based additive manufacturing processes," *Journal of Thermal Science and Engineering Applications*, pp. 1–39, 2022.

[27] T. Dixit, E. Al-Hajri, M. C. Paul, P. Nithiarasu, and S. Kumar, "High performance, microarchitected, compact heat exchanger enabled by 3d printing," *Applied Thermal Engineering*, vol. 210, p. 118339, 2022.

[28] E. Klein, J. Ling, V. C. Aute, Y. Hwang, and R. Radermacher, "A review of recent advances in additively manufactured heat exchangers," *International Refrigeration and Air Conditioning Conference*, 2018.

[29] P. Cova, D. Santoro, D. Spaggiari, F. Portesine, F. Vaccaro, and N. Delmonte, "Cfd modeling of additive manufacturing liquid cold plates for more reliable power press-pack assemblies," *Microelectronics Reliability*, vol. 114, p. 113734, 2020.

[30] C. İ. Çalışkan, M. Coşkun, G. Özer, E. Koç, T. A. Vurkır, and G. Yöndem, "Investigation of manufacturability and efficiency of micro channels with different geometries produced by direct metal laser sintering," *The International Journal of Advanced Manufacturing Technology*, vol. 117, no. 11, pp. 3805–3817, 2021.

[31] A. Elkholy, M. Rouby, and R. Kempers, "Characterization of the anisotropic thermal conductivity of additively manufactured components by fused filament fabrication," *Progress in Additive Manufacturing*, vol. 4, no. 4, pp. 497–515, 2019.

[32] G. Sciacca, M. Sinico, G. Cogo, D. Bigolaro, A. Pepato, and J. Esposito, "Experimental and numerical characterization of pure copper heat sinks produced by laser powder bed fusion," *Materials & Design*, vol. 214, p. 110415, 2022.

[33] M. R. Campagnoli, M. Galati, and A. Saboori, "On the processability of copper components via powder-based additive manufacturing processes: Potentials, challenges and feasible solutions," *Journal of Manufacturing Processes*, vol. 72, pp. 320–337, 2021.

[34] F. Singer, D. Deisenroth, D. Hymas, and M. Ohadi, "Additively manufactured copper components and composite structures for thermal management applications," in *2017 16th IEEE Intersociety Conference on Thermal and Thermomechanical Phenomena in Electronic Systems (ITherm)*, pp. 174–183, IEEE, 2017.

[35] G. Singh, J.-M. Missiaen, D. Bouvard, and J.-M. Chaix, "Copper additive manufacturing using mim feedstock: adjustment of printing, debinding, and sintering parameters for processing dense and defectless parts," *The International Journal of Advanced Manufacturing Technology*, vol. 115, no. 1, pp. 449–462, 2021.

[36] M. Sinico, S. D. Jadhav, A. Witvrouw, K. Vanmeensel, and W. Dewulf, "A micro-computed tomography comparison of the porosity in additively fabricated cucr1 alloy parts using virgin and surface-modified powders," *Materials*, vol. 14, no. 8, p. 1995, 2021.

[37] M. T. F. Thafarallah, W. A. N. W. Mohamed, N. A. Nordin, and H. R. B. A. Razak, "High resolution micro-computed tomography imaging and modelling of porous copper sample," in *2014 IEEE International Conference on Control System, Computing and Engineering (ICCSCE 2014)*, pp. 466–471, IEEE, 2014.

[38] J. Jin, C.-L. Lin, J. D. Miller, C. Zhao, and T. Li, "X-ray computed tomography evaluation of crushed copper sulfide ore for pre-concentration by ore sorting," *Mining, Metallurgy & Exploration*, vol. 39, no. 1, pp. 13–21, 2022.

[39] S. Mohd, J. Abdullah, M. R. Shari, *et al.*, "Comparison types of filter used in viewing inner structure of materials using x-ray computed tomography," 2011.

[40] A. Townsend, L. Pagani, P. Scott, and L. Blunt, "Areal surface texture data extraction from x-ray computed tomography reconstructions of metal additively manufactured parts," *Precision Engineering*, vol. 48, pp. 254–264, 2017.

[41] F. Kim, H. Villarraga-Gómez, and S. Moylan, "Inspection of embedded internal features in additive manufactured metal parts using metrological x-ray computed tomography," in *American Society for Precision Engineering 2016 Summer Topical Meeting*, vol. 64, pp. 191–195, 2016.

[42] Markforged, "Metal x design guide," 2022. `https://3d.markforged.com/white-paper-metal-design-guide.html`, Last accessed on 2022-12-12.

[43] Markforged, "Material datasheet - copper," 2022. `https://www-objects.markforged.com/craft/materials/Copper-V1.1.pdf`, Last accessed on 2022-12-12.

[44] Netzsch, "Light flash apparatus lfa 467 hyperflash - method, technique, applications of thermal diffusivity and thermal conductivity," 2023. https://photos.labwrench.com/equipmentManuals/18086-6393.pdf, Last accessed on 2023-01-15.

[45] Wika, "Model o-10 pressure sensor," 2022. https://www.wika.com/media/Data-sheets/Pressure/Pressure-sensors/ds_pe8165_en_co.pdf, Last accessed on 2023-02-06.

[46] Omega, "Type t thermocouple reference tables," 2022. https://assets.omega.com/pdf/tables_and_graphs/thermocouple-type-t-fahrenheit.pdf, Last accessed on 2023-02-06.

[47] Optris, "Optris pi400i technical data," 2022. https://www.instrumart.com/assets/datasheet-optris-pi-400i.pdf, Last accessed on 2023-02-06.